applied sciences

MDPI

Article

Insights into the Paleostress Analysis of Heterogeneous Fault-Slip Data by Comparing Different Methodologies: The Case of the Voltri Massif in the Ligurian Alps (NW Italy)

Markos D. Tranos [1,*], Petros G. Neofotistos [1], Sotirios A. Kokkalas [2] and Ghislain L. Tourigny [3]

1 Department of Structural, Historical & Applied Geology, Aristotle University of Thessaloniki, 54124 Thessaloniki, Greece
2 Department of Geology, University of Patras, 26500 Patras, Greece
3 SEMS Exploration, Abidjan 06 BP 1334, Côte d'Ivoire
* Correspondence: tranos@geo.auth.gr

Abstract: One of the most critical stages in fault-slip data stress analysis is separating the fault data into homogeneous subsets and selecting a suitable analysis method for each subset. A basic assumption in stress tensor computations is that fault activations occur simultaneously under a homogeneous stress regime. With that rationale, this work aims to attain improvements in the paleostress reconstruction from the polyphase deformed region of Voltri Massif in the Ligurian Alps by using already published heterogeneous fault-slip data inverted using best-fit stress inversion methods and in the absence of any tectonostratigraphic and overprinting criteria. The fault-slip data are re-examined and analyzed with a best-fit stress inversion method and the Tensor Ratio Method (TRM) in the absence of any tectonostratigraphic and overprinting criteria. This analysis defines crucial differences in the paleostress history of the Voltri Massif in the Ligurian Alps, and gives insight into the analysis and results of different stress inversion methodologies. Best-fit site stress tensors have substantial diversity in stress orientations and ratios, implying possible stress perturbations in the region. The reason for these diversities is that the Misfit Angle (MA) minimization criterion taken into account in the best-fit stress inversion methods allows for acceptable fault-slip data combinations, which under the additional geological compatibility criteria used by the TRM, are found to be incompatible. The TRM application on this already published and analyzed data defines similar site and bulk stress tensors with fewer diversities in stress orientations and ratios defined from fault-slip data whose orientations always satisfy the same additional geological compatibility criteria induced by the TRM, and not only from the MA minimization criterion. Thus, TRM seems to define stress tensors that are not as sensitive to the input of fault-slip data, compared to the best-fit stress tensors that appear to suffer from the 'overfitting' modeling error. Five distinct TRM bulk paleostress tensors provide a more constrained paleostress history for the Voltri Massif and the Ligurian Alps, which after the restoration of the ~50° CCW rotation, comprise: (a) a transpression–strike-slip stress regime (T1) with NNE-SSW contraction in Late Eocene, (b) an Oligocene NW-SE extensional regime (T2), which fits with the NW-SE extension documented for the broader area north of Corsica due to a significant change in subduction dynamics, (c) a transient, local, or ephemeral NE-SW transtension (T3) which might be considered a local mutual permutation of the T2 stresses, and (d) a Miocene transpression with a contraction that progressively shifted from ENE-WSW (T4) to NNE-SSW (T5), reflecting the stress reorganization in the Ligurian Alps due to a decrease in the retreating rate of the northern Apennines slab. Therefore, paleostress reconstruction can be fairly described by enhanced Andersonian bulk stress tensors, and requires additional geological compatibility criteria than the criteria and sophisticated tools used by the best-fit stress inversion methods for separating the fault-slip data to different faulting events.

Keywords: fault-slip data; stress inversion; Tensor Ratio Method (TRM); 'enhanced' Andersonian tensors; Ligurian Alps; Northwest Italy

Citation: Tranos, M.D.; Neofotistos, P.G.; Kokkalas, S.A.; Tourigny, G.L. Insights into the Paleostress Analysis of Heterogeneous Fault-Slip Data by Comparing Different Methodologies: The Case of the Voltri Massif in the Ligurian Alps (NW Italy). *Appl. Sci.* **2022**, *12*, 10098. https://doi.org/10.3390/app121910098

Academic Editor: Fabrizio Balsamo

Received: 13 September 2022
Accepted: 4 October 2022
Published: 8 October 2022

1. Introduction

The 'inverse problem', i.e., finding the driving best-fit stress tensor of a given fault population, has been central to the geological community for at least 40 years. Only four parameters, i.e., the orientations of the three principal stress axes (σ_1, σ_2, and σ_3) and the stress ellipsoid shape ratio $R = (\sigma_2 - \sigma_3)/(\sigma_1 - \sigma_3)$ with $0 \leq R \leq 1$ [1,2] are needed to obtain the driving stress tensor. Using numerous stress inversion algorithms with the aid of available software can quickly solve the inverse problem, e.g., [1–12]. Despite the debate on whether the determined principal stress axes represent strain (kinematics) or stress (dynamics) (cf. [13]), there is an increasing number of methods for interpreting fault-slip data and calculating the driving stress tensors. The solutions are mathematically robust and not time-consuming for best-fit stress inversion methods, since they require at least four differently oriented fault planes with slickenlines [1,14]. Nonetheless, they are geologically admissible only if the following fundamental assumptions are satisfied, e.g., [2,3]: (1) The fault-slip data are homogeneous, i.e., they have been activated simultaneously under the same regional stress regime, (2) the orientation of the fault planes is random, (3) displacements on the fault planes are small concerning their lengths, (4) there are no rotations of the fault planes, and (5) slips on the fault planes are independent, and therefore, there is no fault interaction.

Best-fit stress inversion algorithms, e.g., [3,5], were deployed to define the four parameters of the driving stress tensor without having any limitation in the orientation of the stress axes. However, they have been based on the analysis of [15], which is carried out with a stress tensor, having one of its principal stress axes in a vertical position, like the Andersonian model [16]. More precisely, [15] evidenced that any fault slip, even an oblique-slip one, coinciding with the maximum shear stress, i.e., the Wallace-Bott hypothesis [15,17], can be driven by a stress state with a vertical principal stress axis depending only on the stress ratio R.

Despite some arguments about the validity of the Wallace-Bott hypothesis (e.g., [18–21], the 'enhanced' Andersonian model with the addition of the stress ratio succeeds in describing any fault activation, even those driven by transpressional (TRP) or transtensional (TRN) stress regimes, without the need for the principal stress directions to rotate away from the recommended positions of [16,22,23]. Moreover, [24–26] presented a theoretical analysis, i.e., the Slip Preference Analysis (SPA), which indicates the geometry and kinematics of all possible optimal fault planes and their activations under the different enhanced Andersonian states of stress, i.e., extension, compression, and strike-slip, enhanced with the stress ratio values. The importance of the Slip Preference Analysis is that it provides additional compatibility criteria for the simultaneously activated faults under the enhanced Andersonian stress regimes, and therefore, the homogeneity of the fault-slip data.

Geoscientists have tried to unravel the paleostress history of many regions by defining the 'mean' or 'average' stress tensors that can better describe and represent the different tectonic events and concomitant fault reactivations over the rock volume investigated (e.g., [27,28]). They use fault-slip data with various orientations recorded at different sites by applying several best-fit stress inversion methods [29–33].

The best-fit stress methods define stress tensors based only on the Misfit Angle (MA) minimization criterion between the observed fault slickenline and slip preference (SP) [24]. Slip preference is a term that refers to the expected (theoretical) fault slip under a stress regime, and in the best-fit stress inversion methods, it is assumed to coincide with the direction and the sense of the maximum resolved shear stress (the Wallace-Bott hypothesis [15,17]). In general, if the MA of each activated fault is less than 20° ([1,34,35] and references therein), the stress tensor solutions are considered satisfactory, though the threshold angle influences the final results of the methods [36].

However, an individual fault might exhibit a polyphase activity in regions with complex tectonic history. As a result, the recorded fault-slip data are heterogeneous (or polyphase). In such cases, it can be quite puzzling to define exactly which faults have co-functioned under the different driving stress regimes with only the MA minimization criterion. This problem remains unsolved when using either the separation of a fault/slip dataset into independent subsets (hard division) [37–39] or not (soft division) [40]. As a result, in the presence of heterogeneous fault-slip data, the estimation of the optimal stress through the application of the best-fit stress inversion methods is difficult to be reached [38] because such solutions might be misleading due to the influence of faults belonging to other phases [36,38]. Such an estimation can be even more precarious, especially when stress tensors are calculated from < 10 fault-slip data, since such solutions can be found even from randomly generated faults [41]. Although the heterogeneous fault-slip data should be classified into homogeneous groups based on field evidence, this is hard to establish in most cases, like the Voltri Massif of the Ligurian Alps. Therefore, additional compatibility criteria based on the relationship between the fault activation and the driving stress regime are needed to separate the fault-slip data into homogeneous groups.

Regardless of the above, the need to define the stresses drifts scientists to analyze their fault-slip data with the available open-source software, making the process and the used software progressively widely accepted. Such widely used best-fit stress inversion methods are provided by the FSA software ([42] and subsequent modifications), which uses the Monte Carlo search method [1] and Win-Tensor software [43]. The process is iterative and repeats until the remaining data cannot define a physically meaningful stress tensor. Several published articles are based on this inversion approach without using tectonostratigraphic criteria, e.g., [29,32].

The study in [32] examined the polyphase brittle deformation in Voltri Massif and suggested a paleostress history using the FSA software [42] to separate heterogeneous fault-slip data into homogeneous groups, and the Win-Tensor software [43] for verifying this grouping. Both software use best-fit stress inversion algorithms. On the other hand, the study in [44], based not only on the MA minimization criterion of the best-fit stress inversion method, but also on additional compatibility criteria induced by the Slip Preference Analysis concerning the fault activations, developed a new separation and stress inversion method, the Tensor Ratio Method (TRM). This fact motivated us to test and examine whether additional compatibility criteria could assist with data separation and provide better resolved stress tensors that can enhance our understanding of polydeformed regions as the Voltri study area.

The purpose of this study is to examine: (1) whether the results concerning the fault activations in the region and the paleostress history deviate or not from that of [32], (2) the efficiency of the differently applied stress inversion methods and the usefulness of implementing different constraining compatibility criteria among the fault-slip data, and (3) a better understanding of the stress regimes as provided by the site and bulk resolved stress tensors.

2. Geological Setting

The Western Mediterranean region (Figure 1a) has experienced a complex tectonic history since the Mesozoic-Cenozoic, involving the opening and destruction of the Late Triassic/Jurassic Ligurian Ocean and west Alpine Tethys through curved-shaped subduction zones of various polarities [45,46]. The Voltri Massif in the Ligurian Alps (Figure 1a) is an HP eclogite-bearing ophiolite domain consisting of a tectonically complex area between the Western Alps and the Northern Apennines. The Western Alps are characterized by a main westward tectonic nappe-stacking [47–49], and the Northern Apennines, by an east/northeastward vergent fold-and-thrust belt [50,51].

In terms of the tectonostratigraphic framework, the Voltri Massif consists of three main tectonic units [52,53]. These units (Figure 1b), i.e., the Erro-Tobio serpentinized lherzolite, the Beigua serpentinite, and the Piedmontese Nappe, are derived from (a) oceanic crust and mantle, (b) a continental margin, and (c) flysch units derived from the sedimentary cover of an oceanic basement [53]. The boundary between the Western Alps and Northern Apennines is marked by the Sestri-Voltaggio Zone [54], which lies east of the Voltri Massif (Figure 1b) and separates the ophiolitic domain of the Ligurian Alps from the Northern Apennines. This zone is 5–6 km wide, forming an N-S strip from Sestri Ponente in the

Ligurian Sea up to Voltaggio in the north [55] (Figure 1b), and it is characterized by complex kinematics related to the main phases of the Alpine orogenesis [56]. It is also referred to as a Sestri-Voltaggio Fault [57] since it records Oligo–Miocene brittle kinematics [58,59].

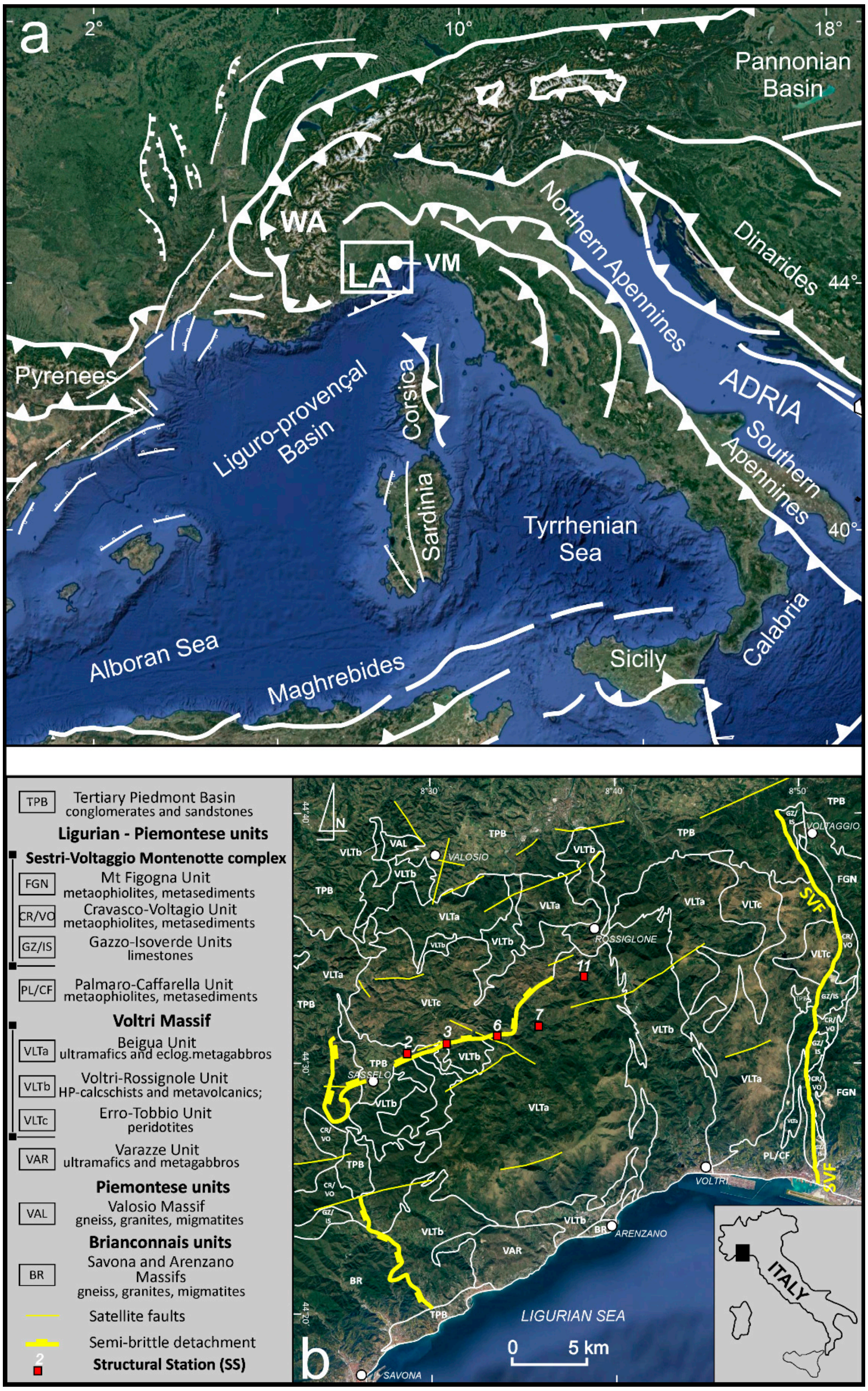

Figure 1. Geographical and geological information concerning the study area: (**a**) Satellite image of the Western-Central Mediterranean (modified from [57] and references therein). Explanation: LA: Ligurian Alps, VM: Voltri Massif, WA: Western Alps. (**b**) Simplified geological map of the Voltri Massif and location of the structural stations (modified after [32,53,55,60]). Explanation: the numbered red squares are the structural stations (SS) with fault-slip data, as presented by [32], SVF: Sestri-Voltaggio Fault.

The present structure of the Apennines resulted from the long-lasting interaction between the African plate or its indenter (i.e., Adriatic-Apulia foreland) and the European plate (Corsica-Sardinia foreland). This interaction involved processes like a Triassic to Early Cretaceous rifting and oceanic spreading, transtension and opening of a young oceanic basin of the Tethyan margin (i.e., the Ligurian-Piedmont ocean), as well as a Late Cretaceous–Early Tertiary eastward intraoceanic subduction that changed polarity to westward subduction in the Paleocene (from Alpine to Apennine) at the European-Adria plate margin [61–64].

Due to the structural position of the Voltri Massif between the two orogens, the Tertiary late-orogenic processes have been described and interpreted differently amongst geoscientists, and the paleostress history remains under debate. This complex scenario is also shown in the evolution of the Tertiary Piedmont Basin (TPB), an Oligo–Miocene wedge-top basin located next to the Voltri Massif and between the two opposite verging orogens (Figure 1). The sedimentation in the TPB occurred in three main tectonic episodes: the exhumation of the Ligurian sector of the Western Alps, the opening of the Liguro-Provençal basin, and the formation of the Apennines thrust belt [57]. In particular, various data show that the brittle-ductile to brittle deformation of both the basement rocks and the TPB deposits was very complex from the Oligocene onwards, since folding and thrusting, as well as normal and strike-slip faulting, were documented, e.g., [58,65–68].

Tectonic reconstructions have interpreted the Voltri Massif as an extensional domain, accommodating lithospheric thinning since the Late Eocene–Early Oligocene [69], or as an exhumed terrain driven by means of polyphase compressional structures [70,71]. The study in [58] attributed the latter to a transpressive regime triggered by the Corsica–Sardinia counterclockwise rotation [69].

In the absence of stratigraphic constraints, the paleostresses and the fault evolution are challenging to unravel. Basement faults (i.e., thrusts) in the Ligurian Alps and North Apennines were active during the Oligo–Miocene and unsealed by the Oligocene transgression [72]. As a result, several tectonic events have been characterized by temporal overlapping and the reactivation of pre-existing structures.

Although detailed studies were carried out in the eastern part of the study area, close to the Sestri Voltaggio Zone (east of the village of Rossiglione; Figure 1b), these provide different conclusions showing the complexity of the brittle-ductile to brittle deformation of the Voltri Massif. In particular, one group of authors [60,73,74] describes the main faults as subvertical, striking N-S, or NW-SE, with strike-slip to oblique-slip kinematics, defining a regional-scale dextral Riedel system, with associated top to the N-NE thrust faults, in the framework of a regional NE-SW trending maximum shortening. The second group describes mainly E-W and N-S or NNW-SSE striking faults, defining pull-apart basins filled with Pliocene sediments during a transtensional stress regime ([75] and references therein).

The study in [60] relates the Voltri Massif with the westward migration of the Alpine thrust front and the contemporaneous eastward retreat of the Apennine slab [76] during the Oligocene-Miocene times. According to [59], two major tectonic complexes exist in the Voltri Massif, separated by a major ductile-to-brittle multiple extensional detachment system (Figure 1b).

In contrast, [71] explains the deformation of the Voltri Massif and the Ligurian Alps with the back-thrust of the Ligurian Alps onto the North Apennine Units. The overall deformation is transpressive in the Oligocene–Miocene times triggered by the Corsica–Sardinia counterclockwise rotation. This transpressive deformation was accommodated by a complex dextral Riedel-type strike-slip fault system, which heavily segmented the Tertiary Piedmont Basin, affecting the sedimentation and the clast provenance of the Tertiary conglomerates.

This complex area of the Voltri Massif where stratigraphic constraints are lacking is used by [32] as a case study to unravel the polyphase brittle tectonics via different stress inversion software on heterogeneous fault-slip data in an area of about 20 km^2. They suggested the following paleostress history of the region since the Oligocene (see Figure 10 of [32]): (a) a

Rupelian–Early Chattian (?) deformation event A, described by a strike-slip tensor with σ_1 trending NNW-SSE, (b) an Aquitanian–Early Burdigalian (?) deformation event B described by a strike-slip tensor with σ_1 trending NE-SW, and (c) a deformation event C described by an extensional/transtensional tensor with σ_3 trending either NW-SE or NE-SW, dated in Pliocene-Quaternary (?).

3. Methods and Fault-Slip Data

Among the several published suggested methods for the stress inversion of fault-slip data (see [23,27,44]), the best-fit stress inversions are still the traditional and most popular in dealing with real data, possibly because of the availability of the open-source software and the fast calculating process itself.

3.1. FSA and Win-Tensor

The driving best-fit stress tensors, determined by [32], were calculated with the aid of the FSA software ([42], and subsequent modifications) and the Win-Tensor software [43], by taking into account MA $\leq 30°$ in SSs shown in Figure 1b. The FSA software first calculates many reduced stress tensors through a random grid search, following the Monte Carlo search method of [1]. The Win-Tensor software initially estimates the parameters of a reduced stress tensor through an improved version of the Right Dihedra method. Afterwards, it defines the optimal stress tensor through an iterative rotational stress optimization process that further minimizes the slip deviations and favors slip on the fault planes [77].

Regarding the application of the Win-Tensor software on their database, the parameters for assessing the stress state's quality are the same as the FSA software, i.e., the MA and its distribution (ideally unimodal) and the high-shear/normal stress ratio. We have to mention that the ratio of shear stress (τ) to normal stress (σ_n) on the fault plane is critical for its (re)activation, and it is called slip tendency T_s [78].

3.2. The Tensor Ratio Method (TRM)

The TRM, as described in [24,25,44], is a simple graphical and semi-automatic method plotting the heterogeneous fault-slip data on TR diagrams and examining if the slips on the faults are simultaneously compatible with a specific orientation of the Andersonian stress axes and a specific stress ratio (R) value (for details, see [44]). Moreover, it can define possible spatial stress perturbations due to large fault structures, as shown in the case of the 1999 Chi-Chi earthquake [25]. The faults with slips characterized by TR compatibility are called Tensor Ratio Compatible Faults (TRCF), defining a specific stress ratio, i.e., the stress ratio of the enhanced Andersonian driving stress tensor. The optimal TRM stress tensor is the one that explains the largest number of the TRCF with MA $\leq 20°$, and secondly, their Mean Misfit Angle (MMA), which must be the smallest. Although in TRM, the default threshold angle for the MA is 20°; in the present examination, for the sake of consistency, we elaborated the optimal TRM stress tensors using MA $\leq 30°$, i.e., the same threshold angle as that chosen by [32].

The TRM uses the MA minimization criterion and additional compatibility criteria concerning the fault activation, as the latter resulted from the Slip Preference Analysis [24–26,44]. More precisely, it has been shown that: (1) extensional and compressional enhanced Andersonian stress regimes could activate, respectively, only extensional and contractional faults; (2) a contractional or an extensional fault can be activated if only its slickenline is in the side where the fault dip direction has an acute angle with the horizontal σ_1 or σ_3 principal stress axis, respectively; (3) faults with dip directions at angles up to $\pm 15°$ with the horizontal principal stress axis, either σ_1 or σ_3, activate as dip-slip faults (either reverse or normal), and these faults have the highest slip tendency values; (4) the (sub)horizontal kinematic axes (either P or T) of the faults with pitch (pt) $\geq 80°$, trend along the horizontal σ_1 or σ_3 axis, and the faults with pt $\geq 60°$ trend very closely around it; and (5) enhanced Andersonian stress regimes, either extensional or compressional, of similar orientations but of different stress ratios activate different Tensor Ratio Compatible Faults with Slip Preferences outlining different plot regions on the TR diagrams.

3.3. Fault Slip-Data

In the present study, fault-slip data (Appendix A) used by [32] for defining the paleostress history in the Voltri Massif of the Ligurian Alps (Figure 1a) are re-analyzed for un-raveling the paleostress history through a different approach. They are 92 fault-slip data in total, and they have been recorded in five structural stations (SS), i.e., SS2, SS3, SS6, SS7, and SS11 from Pra' Vallarino to Tiglieta. These SSs are located along an ENE-WSW to NE-SW boundary that separates the overlying Erro-Tobbio Unit in the north from the underlying Beigua Unit in the south (Figure 1b, and SS location details in Figure 2 of [32]). Both units belong to the Voltri Massif, and according to [32], there is no big fault in this area like the Sestri-Voltaggio fault (SVF) (see Figure 1 and Figure 2 in [32]). In contrast, [60] suggested that the contact is a large detachment fault (Figure 1b). From the 92 fault-slip data, only one that dips at less than 50° towards NNW with extensional displacement (FED_1, Appendix A) at SS2 might be similar to the detachment geometry and kinematics.

Fifty-one (51) fault-slip data are extensional, and 41 are contractional, based on whether the slip along the fault surface is uplifting or subsiding the hanging wall against the footwall block, and considering the horizontal plane as a reference level. Interestingly, 56 fault surfaces display pitch (pt) $\leq 30°$, 22 have $30° < \text{pt} < 60°$, and 14 have $\text{pt} \geq 60°$, indicating the predominance of the strike-slip and oblique-slip fault motions over the dip-slip, which in turn does not favor the precise estimation of the least or greatest principal stress axis of the resolved stress tensors. We follow the stress types classification for the stress regimes of [79].

Finally, we chose these data for analysis and applied a different approach by defining both 'site' stress tensors at each SS and 'bulk' stress tensors from the whole fault-slip dataset to compare our results with their results. Furthermore, the two most remote SSs are at a distance of no more than 10 km from each other (Figure 1, and SS location details in Figure 2 of [32]), describing a rock volume that is small compared to the known large structures of the region like the SVF, and far apart from them, so that it can be considered as a small cubical element for the regional stress regimes [18,80].

In this study, the present analysis includes six stages, starting by examining the possible heterogeneity of the fault-slip data [32] at each SS (Figure 1b) by applying another best-fit stress inversion method, i.e., the 'Minimized Shear Stress Variation,' which uses the algorithm of [81,82] with the aid of MyFault software (Table 1). The authors in [81,82], in estimating the regional stresses, made the simplifying assumption that the magnitude of the slip stress on the fault is similar for all faults in the set at the time of slip. Thus, minimizing the variations in slip stress among the faults leads to an overdetermined set of linear equations. These equations are solved using the standard eigenvector method, giving the three principal stresses and their direction. Because the mean stress during the slip is generally unknown, the principal stresses are normalized, assuming that the maximum stress is 1 and the minimum is 0. The stress ratio is equal to intermediate stress. The fault-slip data for which the obtained MA is greater than 30° under the resolved stress tensor were excluded at each station. However, if any of the excluded fault-slip data under the new resolved stress tensor obtain a new MA that is smaller or equal to 30°, they are reconsidered in the final solution.

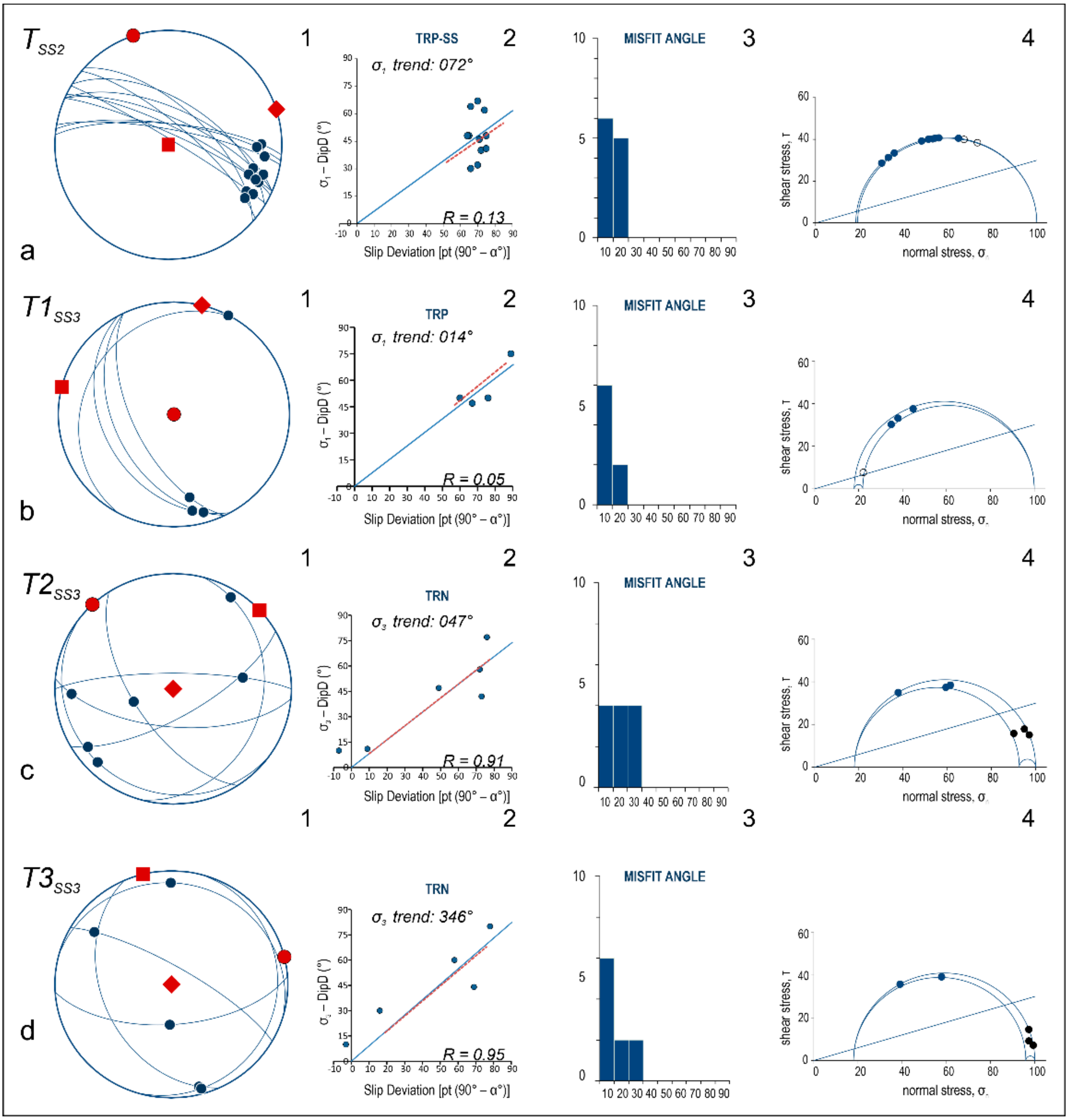

Figure 2. *Cont.*

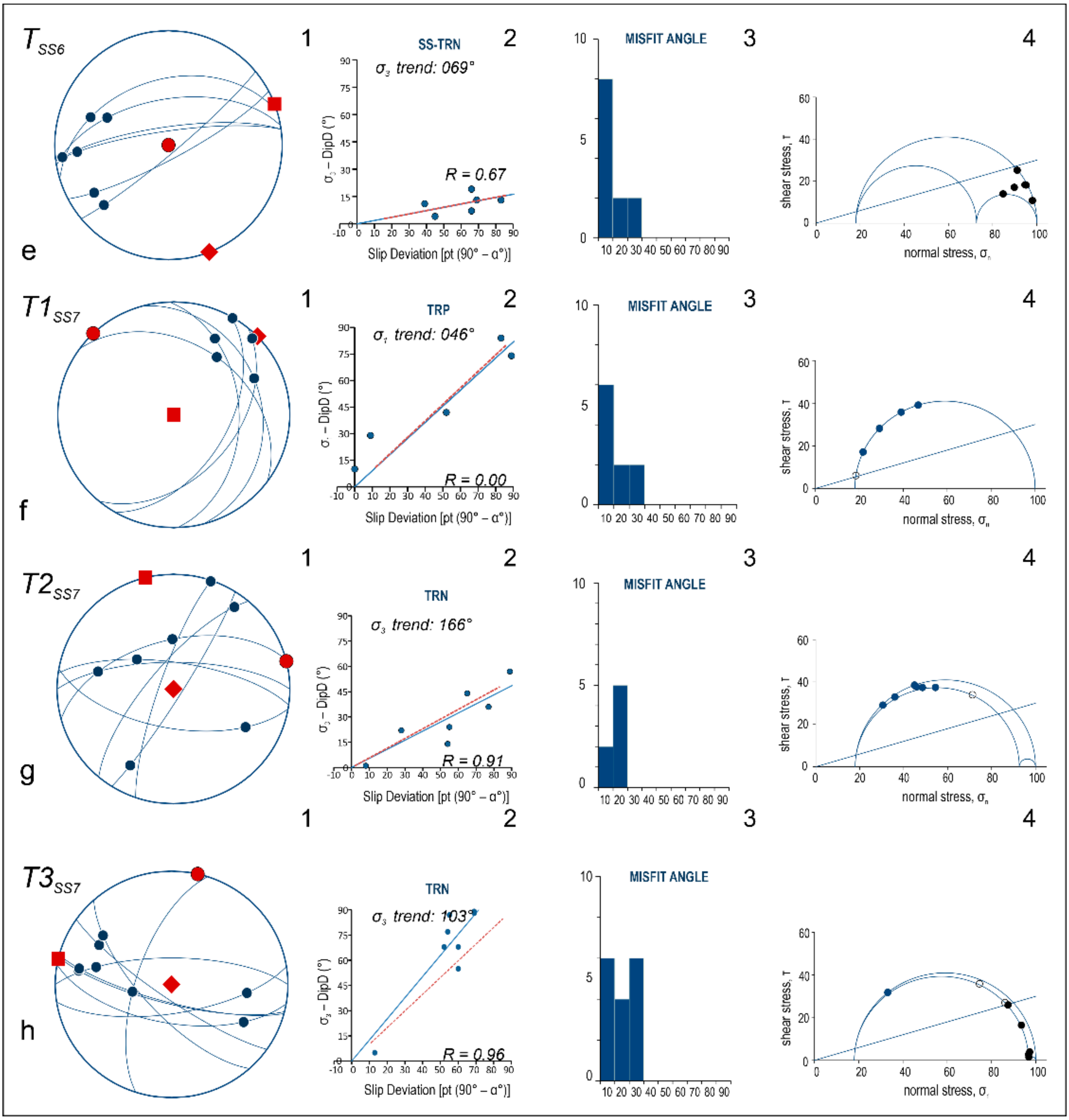

Figure 2. The TRM application [44] to the fault-slip data presented at the different SSs by [32]. The optimal resolved enhanced Andersonian stress tensors (σ_1: solid rhomb, σ_2: solid circle, and σ_3: solid square) (**a**) T_{SS2}, (**b**) $T1_{SS3}$, (**c**) $T2_{SS3}$, (**d**) $T3_{SS3}$, (**e** T_{SS2}, (**f** $T1_{SS7}$, (**g**) $T2_{SS7}$, and (**h**) $T3_{SS7}$ with Misfit Angle (MA) $\leq 30°$. Explanation: 1. Stereographic projection (equal-area, lower hemisphere) of the TR compatible fault-slip data (TRCF), the blue balls are extensional faults in the extensional stress regimes and contractional faults in the compressional stress regimes; 2. TR diagram shows the TRCF (solid blue balls), the 'real' (blue colored line), and 'theoretical' (red dashed line) Final Tensor Ratio Line (FTRL); 3. Misfit Angle (MA) distribution of the TRCF; 4. Mohr diagram of the TRCF. Solid blue balls show the TRCF having $T_s \geq 0.6$. Open balls show the TRCF with $T_s < 0.6$. The blue line shows the lowest initial friction curve at the frictional angle $\varphi = 16.7°$.

Table 1. Best-fit stress tensors with MyFault, software, and MA ≤ 30°.

ST	n	FTC	FTE	σ_1	σ_2	σ_3	R	MMA	FT (MA ≤ 30°)	FT/n (%)	N	N (MA ≥ 30°)	SS
T_MF$_{SS2}$	16	12	4	072°–30°	275°–58°	168°–11°	0.48	28.3°	14	88	1–16	2, 14	SS2
T_MF$_{SS2F}$	14	12	2	065°–22°	293°–60°	164°–20°	0.68	7.0°	14	100			SS2
T_MF$_{SS3}$	21	7	14	268°–78°	082°–12°	173°–01°	0.57	63.8°	6	29	17–37	18,19, 20, 21, 22, 23, 24, 27, 28, 29, 30, 32, 35, 36, 37	SS3
T_MF$_{SS3F}$	6	0	6	274°–84°	081°–05°	171°–01°	0.45	9.8°	6	100		17, 25, 26, 31, 33, 34	SS3
T_MF$_{SS6}$	13	8	5	156°–12°	036°–67°	250°–20°	0.39	63.3°	6	46	38–50	38, 39, 40, 42, 47, 48, 50	SS6
T_MF$_{SS6F}$	6	5	1	154°–04°	052°–72°	245°–17°	0.47	7.1°	6	100			SS6
T_MF$_{SS7}$	32	10	22	258°–57°	151°–11°	055°–31°	0.11	76.8°	5	16	51–82	51, 52, 53, 54, 55, 56, 58, 59, 60, 61. 62, 63, 64, 65, 66, 67, 68, 69, 70, 72, 74, 76, 77, 78, 79, 81, 82	SS7
T_MF$_{SS7F}$	5	1	4	258°–52°	351°–02°	083°–38°	0.39	10.0°	5	100			SS7
T_MF$_{SS11}$	10	4	6	009°–08°	266°–57°	104°–31°	0.53	62.7°	2	20	83–92	83, 84, 85, 86, 87, 90, 91, 92	SS11
T_MF$_{SS11F}$	4	0	4	150°–44°	294°–40°	041°–19°	0.20	3.8°	4	100			SS11

The resolved best-fit site stress tensors at each structural station (SS), e.g., T_MF$_{SS2}$, with the use of the best-fit stress inversion method, “Minimized Shear Stress Variation” that uses the algorithm of [81,82]. Explanation: T_MF$_{SS2}$: Tensor (T), MF (MyFault), SS2: structural station 2, ST: Stress tensor, n: number of fault-slip data in the SS, FTC: contractional fault-slip data, FTE: extensional fault-slip data, R: stress ratio, FT (MA ≤ 30°): Fault-slip data with Misfit Angle ≤ 30°, MMA: Mean Misfit Angle, FT/n: percentage of the fault-slip data that have MA ≤ 30° out of the total number (n), N: The number of the fault-slip datum as shown in Table A1.

4. Paleostress Analysis Results

Table 1 describes the resolved best-fit site stress tensors with MyFault software, verifying the fault-slip data's heterogeneity as stated by [32]. Indeed, all SSs apart from the SS2 include heterogeneous fault-slip data, since the first resolved stress tensors, e.g., T_MF_{SS3}, and T_MF_{SS7}, explain a low percentage of fault-slip data with MA $\leq$ 30°, and the mean Misfit Angle (MMA) is much higher than 20° [83,84]. In SS2, however, the input fault-slip data's heterogeneity shown by the MMA = 28.3° is not real, but is due to the fault-slip data with numbers 2 and 14 (see Appendix A). The latter describes slip vectors with opposite sense of slip, i.e., normal dextral (ND) in contrast to inverse-sinistral (IS) of the others (see Figure 8 in [32]). Excluding the incompatible fault-slip data, i.e., those with MA> 30°, five resolved stress tensors labeled with F, e.g., T_MF_{SS7F} (Table 1), can be accepted as candidate solutions since they explain all the input fault-slip data with MA $\leq$ 30°. However, all these solutions T_MF_{SS*F} have been defined with less than 10 input fault-slip data, apart from the T_MF_{SS2F}. In addition, three out of five, i.e., T_MF_{SS2F}, T_MF_{SS7F} and T_MF_{SS11F}, do not obey the enhanced Andersonian model, implying that the region was subjected to non-Andersonian stress states. The second stage refers to the TRM application on the fault-slip data of each SS for defining the enhanced Andersonian site stress tensors, as shown in Table 2 and Figure 2. In four out of five SS, enhanced Andersonian site stress tensors have been obtained (Table 2). In addition, in two SS, i.e., the SS3 and SS7, where more than 20 fault-slip data were recorded, site stress tensors of more than one were calculated. Most of the site stress tensors (except the SS2) were found with less than 10 fault-slip data, as the stress tensors defined by [32] and the 'Minimized Shear Stress Variation' best-fit stress inversion method. Such site stress tensors should be treated with great caution, since the MMA cannot be used as a quality indicator [41,83–85].

The third stage of the analysis includes the calculation of the bulk stress tensors by applying the TRM to the whole fault-slip dataset (Appendix A). The calculation of the bulk stress tensors eliminates possible stress heterogeneities due to the fault interaction or the existence of large structures (see also [29,30,85]). In particular, five bulk stress tensors, labeled $T1_{TRM}$ through $T5_{TRM}$, have been calculated (Figure 3, Table 3).

Table 2. The enhanced Andersonian site stress tensors (MA $\leq$ 30°) with the TRM application [41].

ST	N	FTE	FTC	TRCF	σ_1	σ_2	σ_3	R	ST REG	MMA (MA $\leq$ 30°)	N (Appendix A)	SS
T_{SS2}	16	4	12	11	072°–00°	072°–90°	162°–00°	0.01	TRP-SS	11.1°	3, 4, 5, 7, 8, 9, 10, 12, 13, 15, 16	SS2
$T1_{SS3}$	21	14	7	4	014°–00°	014°–90°	104°–00°	0.05	TRP	9.0°	21, 22, 29, 35	SS3
$T2_{SS3}$	21	14	7	6	047°–90°	137°–00°	047°–00°	0.91	TRN	15.0°	20, 27, 30, 32, 34, 37	SS3
$T3_{SS3}$	21	14	7	5	346°–90°	076°–00°	346°–00°	0.95	TRN	10.6°	17, 23, 28, 31, 33	SS3
T_{SS6}	13	5	8	6	159°–00°	159°–90°	069°–00°	0.67	SS-TRN	12.8°	(40), (41), 43, 44, 45, 46, 48, 49	SS6
$T1_{SS7}$	32	22	10	5	046°–00°	136°–00°	046°–90°	0	TRP	9.4°	53, 57, 58, 62, 64	SS7
$T2_{SS7}$	32	22	10	7	166°–90°	076°–00°	166°–00°	0.91	TRN	14.0°	60, 63, 68, 75, 76, 80, 82	SS7
$T3_{SS7}$	32	22	10	8	103°–90°	013°–00°	103°–00°	0.96	TRN	15.5°	52, 54, 59, 74, 76, 78, 79, 80	SS7

The enhanced Andersonian site stress tensors, as defined at the different structural stations (SS) with the TRM application [44]. Explanation as in Table 1, TRCF: Tensor Ratio Compatible faults, ST REG: stress regime, N: extensional fault-slip data compatible with the TRM stress tensor. TRP: Transpression, SS: (pure) Strike-Slip, TRN: Transtension.

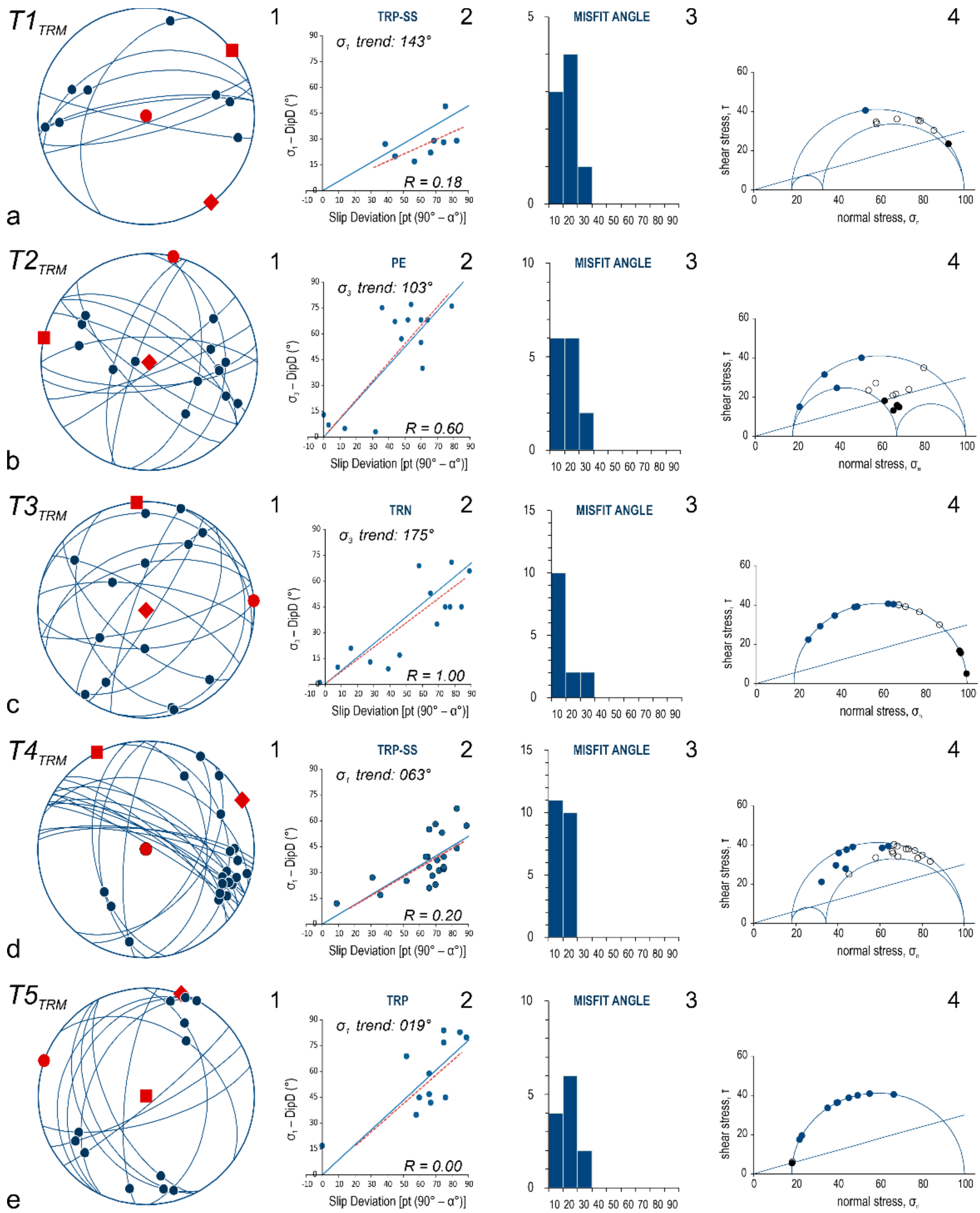

Figure 3. The TRM application [41] to the same fault-slip dataset as presented by [40]. The optimal resolved stress tensors (σ_1: solid rhomb, σ_2: solid circle, and σ_3: solid square) (**a**) $T1_{TRM}$, (**b**) $T2_{TRM}$, (**c**) $T3_{TRM}$, (**d**) $T4_{TRM}$, and (**e**) $T5_{TRM}$, from the whole fault-slip dataset and Misfit Angle (MA) $\leq 30°$. Explanation as in Figure 2.

$T1_{TRM}$ bulk stress tensor is defined by only eight fault-slip data. It explains four fault-slip data in site SS6 and less than four in sites SS7 and SS11. It could be correlated with the T_{SS6} site stress tensor, although a change in the trend of the horizontal stress axis is observed.

$T2_{TRM}$ bulk stress tensor is defined by 14 fault-slip data and explains six fault activations in SS7, four at SS11, and less than four in the other SS.

$T3_{TRM}$ bulk stress tensor is defined by 14 fault-slip data and explains five fault activations in SS3 and seven in SS7. It presents substantial similarity with the site stress tensors $T3_{SS3}$ and $T2_{SS7}$.

$T4_{TRM}$ bulk stress tensor is well defined by 21 fault-slip data and explains 10 fault activations in SS2 and four in SS7, having substantial similarity with the site stress tensors T_{SS2} and $T1_{SS7}$. It also explains less than four fault activations in other sites like SS11.

$T5_{TRM}$ bulk stress tensor is defined by 12 fault-slip data and explains four fault activations in SS3 and less than four in SS6, SS7, and SS11. It presents a strong similarity with the $T1_{SS3}$ site stress tensor.

Since our interest is to compare the TRM with the best-fit stress inversion methods, a fourth analysis stage is performed. In this stage, we examine which additional fault-slip data (Appendix A) are compatible with the enhanced Andersonian bulk stress tensors of the previous stage if we only consider the MA minimization criterion of 30°, i.e., the constraint of the best-fit stress inversion methods used by [32]. All the resolved Andersonian bulk stress tensors, $T1_{TRM}$ through $T5_{TRM}$, now labeled $T1_{all}$ through $T5_{all}$, are consistent with more fault-slip data than those defined by the TRM, and in some SSs, the explained fault-slip data are now equal to or greater than four (Table 4). For example, in SS7, the $T4_{all}$ tensor explains nine instead of four fault-slip data explained by the $T4_{TRM}$, and $T2_{all}$ explains eight instead of six fault-slip data explained by the $T2_{TRM}$; and in SS11, the $T2_{all}$ tensor explains four fault-slip data, although no Andersonian site stress tensor was able to be defined in this SS. In addition, the MMA in each solution is less than 20°. This is a fact that fortifies the fault-slip data homogeneity and that leads to accepted resolved stress tensors.

The fifth analysis stage deals with the fault-slip data explained by the enhanced Andersonian stress tensors, i.e., $T1_{all}$ through $T5_{all}$, since some of the latter define the TRP and TRN stress regimes. Do these fault-slip data define Andersonian or non-Andersonian stress tensors by applying a best-fit stress inversion method (i.e., a method with no limitation of having one principal stress axis in a vertical position)?

The 'Minimized Shear Stress Variation,' based on the algorithm of [81,82], defines stress tensors labeled $T1_{MF}$ to $T5_{MF}$ (Figure 4, Table 5). The resolved best-fit stress tensor, $T5_{MF}$, defined by the same fault-slip data with the minimization criterion MA $\leq$ 30° and almost the same MMA, is non-Andersonian, i.e., having its principal stress axes plunging less than 65° [86].

In the final part of our analysis (sixth stage), we tackle another issue concerning the above-described $T1_{all}$ through $T5_{all}$ stress tensors. It concerns the degree of similarity among the resolved stress tensors. This issue has been pointed out by [44,83,84], who suggested the comparison and the degree of similarity between two resolved stress tensors A and B with the use of the Stress Tensor Discriminator Faults (STDF), i.e., the faults which were activated by either A or B stress tensor, but not from both. In particular, three percentages of the Stress Tensor Discriminator Faults are calculated: one for the AB fault-slip dataset, and the other for the A and B fault-slip datasets, respectively. None of the calculated enhanced Andersonian bulk stress tensors are similar, since the percentages of the STDFs are above 80% (Table 6), suggesting that they define distinct stress regimes that should be explained from a geological point of view.

Table 3. The enhanced Andersonian bulk stress tensors with the TRM application [41].

ST	N	FTE	FTC	TRCF	σ_1	σ_2	σ_3	R	ST REG	MMA (MA ≤ 30°)	N (Appendix A)	SS
$T1_{TRM}$	92	51	41	8	143°–00°	143°–90°	053°–00°	0.18	TRP-SS	13.0°	**43**, **44**, **45**, **46**, 69, 72, 77, 87	**SS6 (4)**, SS7 (3), SS11 (1)
$T2_{TRM}$	92	51	41	14	103°–90°	013°–00°	103°–00°	0.60	PE	13.4°	14, 25, 26, 40, **52**, **54**, **59**, **70**, **74**, **80**, **86**, **89**, **90**, **91**	SS2 (1), SS3 (2), SS6 (1), **SS7 (6)**, **SS11 (4)**
$T3_{TRM}$	92	51	41	14	175°–90°	085°–00°	175°–00°	1.00	TRN	9.6°	1, **17**, **23**, **28**, **31**, **33**, 39, **60**, **63**, **65**, **68**, **73**, **75**, **82**	SS2 (1), **SS3 (5)**, SS6 (1), **SS7 (7)**
$T4_{TRM}$	92	51	41	21	063°–00°	063°–90°	153°–00°	0.20	TRP-SS	11.4°	**3**, **4**, **5**, **7**, **8**, **9**, **10**, **12**, **13**, **15**, **16**, 18, 36, 42, **57**, **58**, **62**, **64**, 83, 84, 85	**SS2 (11)**, SS3 (2), SS6 (1), **SS7 (4)**, SS11 (3)
$T5_{TRM}$	92	51	41	12	019°–00°	109°–00°	019°–90°	0.00	TRP	13.1°	**21**, **22**, **29**, **35**, 47, 48, 49, 53, 58, 61, 85, 87	**SS3 (4)**, SS6 (3), SS7 (3), SS11 (2)

The enhanced Andersonian bulk stress tensors, as defined at the different structural stations (SS) with the TRM application [44]. Explanation as in Tables 1 and 2; fault-slip data ≥ 4 are shown in bold as the SSs, where they were recorded. TRP: Transpression, SS: (pure) Strike-Slip, TRN: Transtension. PE: Pure Extension.

Table 4. The activated fault-slip data under the bulk enhanced Andersonian stress tensors with MA ≤ 30°.

ST	N	σ_1	σ_2	σ_3	R	ST REG	MMA (MA ≤ 30°)	FT (MA ≤ 30°)	N (Appendix A)	SS
T1all	92	143°–00°	143°–90°	053°–00°	0.18	TRP-SS	16°	18	14, 23, 41, 43, 44, 45, 46, 50, 52, 54, 69, 72, 77, 78,79, 87, 91, 92	SS2 (1), SS3(1), **SS6 (6)**, **SS7 (7)**, SS11 (3)
T2all	92	103°–90°	013°–00°	103°–00°	0.60	PE	13.5°	19	14, 25, 26, 33, 34, 38, 40, 52, 54, 59, 66, 70, 74, 75, 80, 86, 89, 90, 91	SS2 (1), **SS3 (4)**, SS6 (2), **SS7 (8)**, **SS11 (4)**
T3all	92	175°–90°	085°–00°	175°–00°	1.00	TRN	14°	22	1, 9, 17, 19, 23, 28, 30, 31, 33, 38, 39, 60, 62, 63, 65, 68, 73, 75, 76, 82, 85, 90	SS2 (2), **SS3 (7)**, SS6 (2), **SS7 (9)**, SS11 (2)
T4all	92	063°–00°	063°–90°	153°–00°	0.20	TRP-SS	12.4°	27	3, 4, 5, 7, 8, 9, 10, 12, 13, 15, 16, 18, 36, 38, 42, 57, 58, 60, 62, 63, 64, 65, 70, 82, 83, 84, 85	**SS2 (11)**, SS3 (2), SS6 (2), **SS7 (9)**, SS11 (3)
T5all	92	019°–00°	109°–00°	019°–90°	0.00	TRP	15.5°	17	3, 4, 21, 22, 29, 35, 38, 47, 48, 49, 53, 58, 61, 66, 85, 87, 88	SS2 (2), **SS3 (4)**, **SS6 (4)**, **SS7 (4)**, SS11 (3)

The activated fault-slip data under the resolved bulk enhanced Andersonian stress tensors, namely $T1_{all}$ through $T5_{all}$, considering only the MA≤ 30° criterion used in the best-fit stress inversion methods. TRP: Transpression, SS: (pure) Strike-Slip, TRN: Transtension. PE: Pure Extension. Explanation as in Tables 1–3.

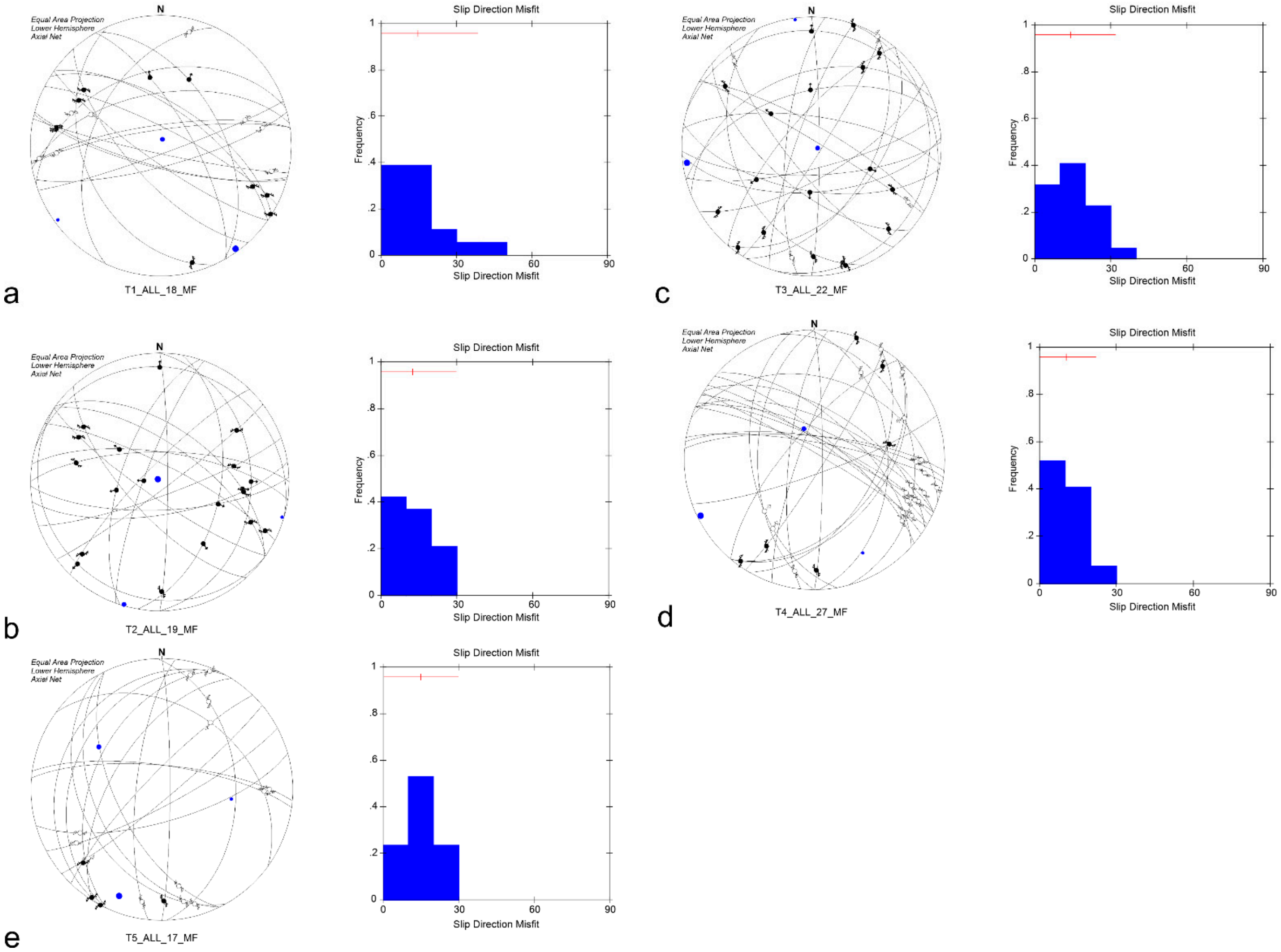

Figure 4. The application of the "Minimized Shear Stress Variation" best-fit stress inversion method with the aid of the software MyFault, which uses the algorithm of [81,82] on the $T1_{all}$ through $T5_{all}$ fault-slip data. (**a**–**e**) Stereographic projections and Misfit Angle (MA) histograms for the $T1_{MF}$ through $T5_{MF}$ resolved stress tensors. Explanation: The principal stress axes of the resolved stress tensor are shown with solid circles (maximum: biggest solid circle, intermediate: solid middle circle, and minimum: smallest solid circle). In the uppermost part of the MA histogram, the thin horizontal line centered on the mean shows the Mean Misfit Angle (MMA) and has a length equal to twice the 95% confidence value.

Table 5. Best-fit stress tensors from the fault-slip data driven by the enhanced Andersonian bulk stress tensors.

ST	n	σ_1	σ_2	σ_3	R	ST REG	MMA (MA ≤ 30°)	FT (MA ≤ 30°)	N (Appendix A)	SS
$T1_{MF}$	18	144°–03°	014°–86°	234°–03°	0.46	SS	14.6°	16	14, 41, 43, 44, 45, 46, 50, 52, 69, 72, 77, 78,79, 87, 91, 92	SS2 (1), **SS6 (6)**, **SS7 (6)**, SS11 (3)
$T2_{MF}$	19	321°–88°	196°–01°	106°–02°	0.60	PE	12.6°	19	14, 25, 26, 33, 34, 38, 40, 52, 54, 59, 66, 70, 74, 75, 80, 86, 89, 90, 91	SS2 (1), **SS3 (4)**, SS6 (2), **SS7 (8)**, **SS11 (4)**
$T3_{MF}$	22	263°–04°	105°–86°	353°–02°	0.84	SS-TRN	14.2°	21	1, 9, 17, 19, 23, 28, 30, 31, 33, 38, 39, 60, 62, 63, 65, 68, 73, 75, 76, 82, 85, 90	SS2 (2), **SS3 (7)**, SS6 (2), **SS7 (9)**, SS11 (2)
$T4_{MF}$	27	244°–03°	341°–69°	153°–20°	0.29	TRP-SS	10.4°	27	3, 4, 5, 7, 8, 9, 10, 12, 13, 15, 16, 18, 36, 38, 42, 57, 58, 60, 62, 63, 64, 65, 70, 82, 83, 84, 85	**SS2 (11)**, SS3 (2), SS6 (2), **SS7 (9)**, SS11 (3)
$T5_{MF}$	17	202°–13°	304°–41°	098°–45°	0.16		15.1°	17	3, 4, 21, 22, 29, 35, 38, 47, 48, 49, 53, 58, 61, 66, 85, 87, 88	SS2 (2), **SS3 (4)**, **SS6 (4)**, **SS7 (4)**, SS11 (3)

The resolved bulk stress tensors after applying the best-fit stress inversion method, "Minimized Shear Stress Variation," which uses the algorithm of [81,82] onto the $T1_{all}$ through $T5_{all}$ fault-slip data. TRP: Transpression, SS: (pure) Strike-Slip, TRN: Transtension. PE: Pure Extension. Explanation as in Tables 1–3.

Table 6. Similarity between the enhanced Andersonian bulk stress tensors.

STDF(%)	T2all	T3all	T4all	T5all
T1all	(87.9)(77.8)(78.9)	(97.4)(94.4)(95.5)	(100)(100)(100)	(97.1)(94.1)(94.4)
T2all		(89.2)(81.8)(78.9)	(95.5)(92.6)(89.5)	(94.1)(88.2)(89.5)
T3all			(80.5)(70.4)(63.6)	(94.6)(88.2)(90.9)
T4all				(87.2)(81.5)(70.6)

Comparison between the calculated stress tensors (e.g., A and B) of the present analysis using the TRM [44]. The comparison is carried out using a priori the Stress Tensor Discriminator Faults (STDF) [44,83,84] and an MA ≤ 20°. The bracketed numbers in rows show the percentages of the STDF of the dataset driven by AB, A, and B stress tensors, respectively. A: The stress tensors in rows; B: the stress tensors in columns.

5. Structural Interpretation—Discussion

5.1. Insight into the Paleostress Analysis from Previous Approaches

The paleostress analysis presented by [32] deals with fault-slip data that have been recorded in ultramafic rocks, i.e., rocks easily fractured, forming fault rocks as reported by [32], making the 'no-fault interaction' assumption of the stress inversion methods highly uncertain, especially in the limited spatial scale of the SSs. When heterogeneous fault-slip data are recorded in an SS of limited spatial scale, there is always the question of whether the slip independence among the recorded fault-slip data are valid. This is especially true for fault planes interconnected to each other and that are part of a prominent fault structure or a fault zone, a fact that strongly influences the validity of the stress inversion techniques [80].

The resolved best-fit site stress tensors of [32] are characterized by considerable diversity in the orientation of the principal stress axes and the stress ratio (see their Figure 5). Similar results have been found in our first analysis stage by applying the [81,82] best-fit stress inversion method with the aid of MyFault software. However, the very small number of the fault-slip data, i.e., < 6 fault-slip data, from which these tensors were defined, constitutes these solutions as potentially resulting from randomly generated faults [36].

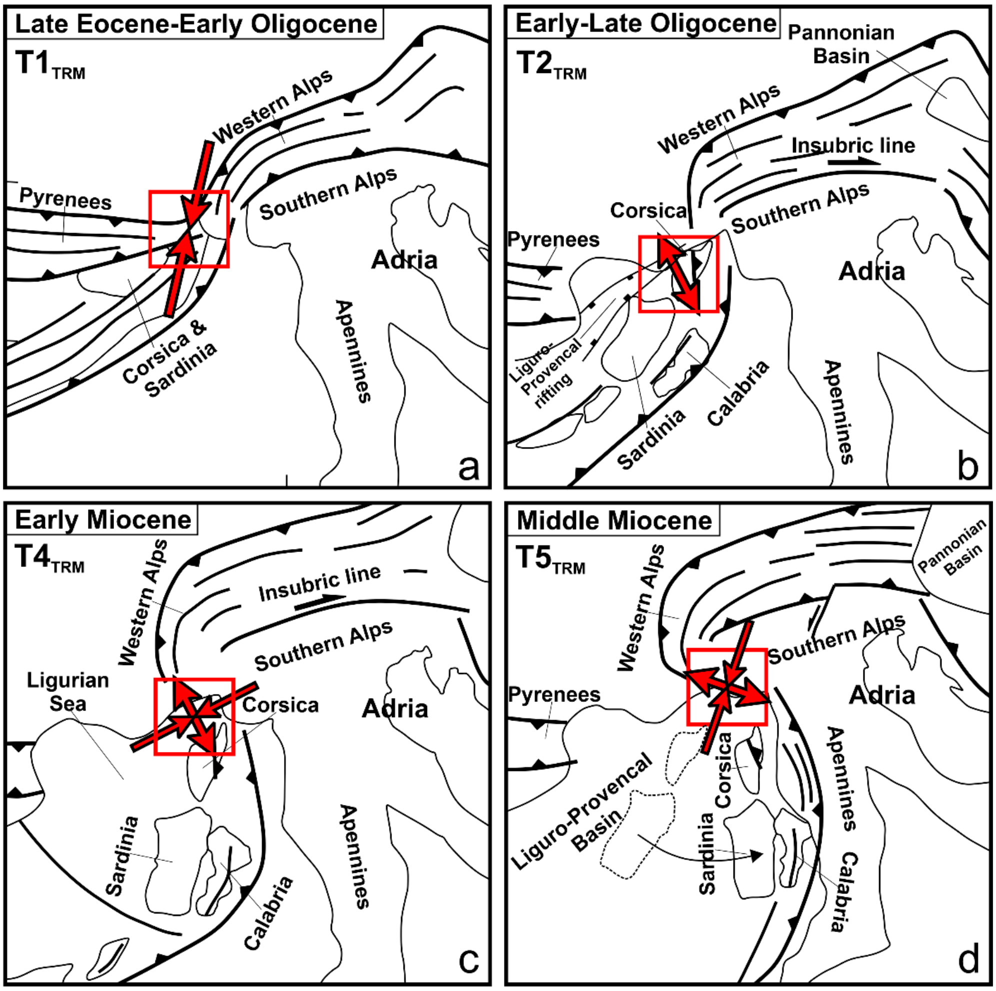

Figure 5. Tectonic setting of the Central-Western Mediterranean (based and modified from [45]) and paleostress reconstruction of the Ligurian Alps (NW Italy) (red square) since the Late Eocene, considering the 50° counterclockwise rotation that occurred in Early–Middle Miocene [32,69]. (**a**) $T1_{TRM}$ (restored) (**b**) $T2_{TRM}$ (restored), (**c**) $T4_{TRM}$, and (**d**) $T5_{TRM}$. Explanation: σ_1 and σ_3 axes are shown with convergent and divergent arrows, respectively.

Any resolved site stress tensor calculated mathematically with a best-fit stress inversion software results in a specific combination of fault activations. As a result, it is not only the stress regime, but also the fault activations that should be geologically reasonable and plausible. Are these fault activation combinations similar when determined by different software? As shown in Figure 5 of [32], in the SS3 station (3—N of Palo), the Andersonian and non-Andersonian tensors, T1 and T2, respectively (as derived using FSA), are grouped in the same event B, whereas with Win-Tensor software, the resolved stress tensors have been grouped differently due to different fault combinations.

In a more detailed inspection of the above-mentioned best-fit stress tensors, it is evident that they can be either Andersonian or not, considering if the steepest plunging principal stress axis plunges $\geq 65°$ or not, respectively (cf. [86]). Nonetheless, in most cases, the non-Andersonian stress tensors have their greatest or least principal stress axes in a (sub)horizontal position. An explanation for this is that the four components of the reduced stress tensor are defined using best-fit algorithms simultaneously but independently from one another, and without having any physical, and therefore, geological constraints or limitations concerning the position of the principal stress axes. However, non-Andersonian stress tensors can be falsely resolved from fault-slip data if the latter are heterogeneous [85] or mixed in kinematics, i.e., dip-slip (thrust or normal), oblique, and strike-slip faults driven by transpressional *s.l.* stress regimes. It is worth noting that in TRP or TRN, where $R \leq 0.125$ and $R \geq 0.875$, respectively [79], it is not important which of the two principal stress axes is in a vertical position, since their magnitudes are very close, if not equal, making it trivial as to whether the resolved stress type is Andersonian or not.

Another issue is that the variations in the orientations of the stresses and stress ratios of the best-fit site stress tensors imply strong stress perturbations for the region. Unfortunately, in such cases, stress perturbations cannot be established based solely on the best-fit stress inversion methods at the different SSs in the case of heterogeneous fault-slip data [85].

The iterative process followed in the FSA and Win-Tensor software in each SS results in calculating, solely and strictly, the first stress tensor from the original fault-slip data. In contrast, the next resolved stress tensors are biased to different degrees, since they were calculated from successively nested datasets, i.e., smaller in number than the original dataset, especially if the SS is of limited spatial scale. Moreover, this inconsistency cannot be seen by the best-fit stress resolved site stress tensors themselves if the latter are diverse in terms of the orientation of the stresses and the stress ratios due to the different input fault-slip data combinations recorded at the different SSs.

5.2. Insight into the TRM Site and Bulk Enhanced Andersonian Stress Tensors

The TRM application calculates enhanced Andersonian site stress tensors in all SSs, except for SS11. Most define TRP and TRN stress regimes, as implied by the predominance of the strike-slip and oblique-slip faults in the study area. In cases where the site stress tensors were calculated from less than 10 fault-slip data, they present differences in the horizontal stress axis orientation like the pairs ($T1_{SS3}$, T_{SS6}) and ($T3_{SS3}$, $T2_{SS7}$) (Table 2).

The TRM application on the whole fault-slip dataset (Appendix A) defines five bulk stress tensors, $T1_{TRM}$, through $T5_{TRM}$ (Table 3). Apart from the first, the other bulk stress tensors were calculated with more than 10 fault-slip data, i.e., the minimum number to overcome randomly defined stress tensors [41]. These bulk stress tensors can activate more than four differently oriented fault-slip data in a few SS, and fault-slip data from several SS having similar attitudes, as in the case of similar fault activations recorded through focal mechanisms at different sites in seismically active areas, e.g., [87]. In addition, from Tables 2 and 3, it seems that both TRM site and bulk stress tensors define similar stress regimes like (a) $T1_{TRM}$ with T_{SS6}, (b) $T2_{TRM}$ with $T3_{SS7}$, (c) $T3_{TRM}$ with $T3_{SS3}$ and $T2_{SS7}$, (d) $T4_{TRM}$ with T_{SS2} and $T1_{SS7}$, and (e) $T5_{TRM}$ with T1SS3. This similarity occurs because the TRM stress tensors are calculated from the Tensor Ratio Compatible Faults regardless of the number of fault-slip data [44,85].

The interesting issue is that all the resolved enhanced Andersonian site stress tensors define transpressional *s.l.* stress regimes, i.e., those that fit well with the predominance of subhorizontal to oblique-slip faults over the dip-slip faults [24–26] in the recording dataset mentioned. Therefore, the enhanced Andersonian stress tensors can fairly describe transpression *s.l.* stress regimes.

When the minimization criterion of $MA \leq 30°$ was only considered, the TRM bulk stress tensors explained more fault-slip data out of the whole fault-slip dataset than those defined by the TRM application (see $T1_{all}$ through $T5_{all}$ in Table 4). Because of the large number of the explained fault-slip data, these solutions can hardly be considered to be a result of combining random fault-slip data by taking into account only the MA minimization criterion used by the best-fit stress inversion methods. For example, the $T1_{all}$ stress tensor explains 10 more fault-slip data than $T1_{TRM}$. In addition, when a best-fit stress inversion method was applied to the fault-slip data explained by the $T1_{all}$ to $T5_{all}$ tensors, the resolved bulk stress tensors $T1_{MF}$ through $T5_{MF}$, apart from the $T5_{MF}$, did not differ significantly from the $T1_{all}$ through the $T5_{all}$, respectively (Tables 4 and 5). Apart from the $T5_{MF}$, all the tensors define one principal stress axis at $\leq 25°$ from the vertical position following Anderson's assumed 'standard state' stress configuration near the Earth's free surface [88]. On the other hand, considering the $T5_{MF}$, someone might promptly conclude that the driving stress regime in the region might be of non-Andersonian type. However, the

Andersonian standard state of stress is also supported by the paleomagnetic data in the region and, more precisely, the inclination values calculated by [69], which in their majority show no significant rotations (<10°) around the horizontal axes. As a result, both the Andersonian ($T5_{all}$) and the non-Andersonian ($T5_{MF}$) stress tensors explain the same fault-slip data with the minimization criterion MA $\leq 30°$ and almost the same MMA. However, the enhanced Andersonian tensor $T5_{all}$ is more admissible for the region, suggesting that the enhanced Andersonian stress tensors can fairly describe the faulting deformation in a region, even if the latter is subjected to transpression *s.l.* tectonics.

5.3. Remarks on Comparing the Methods

The detailed re-examination of these fault-slip data with the TRM application, which uses additional constraints induced using Slip Preference Analysis, likewise defines TRM site stress tensors with less than 10 fault-slip data [32] and TRM bulk stress tensors with more than 10 fault-slip data (except for $T1_{TRM}$, which was calculated from eight fault-slip data). However, the TRM site and bulk stress tensors are quite similar and not diverse, in terms of stress axis orientation and stress ratio, as those calculated from the best-fit stress inversion methods. It also indicates that the TRM defines stress tensors that are not as sensitive to the input fault-slip data as the best-fit stress tensors are. Thus, we can argue that the best-fit stress inversion methods suffer from the 'overfitting' modelling error, which is more limited in the TRM application due to the additional SPA geological constraints [24–26].

More importantly, the resolved bulk stress tensors obtained from the TRM were determined exactly from the same original fault-slip dataset. These TRM bulk stress tensors were defined with much more than 10 fault-slip data, indicating that these solutions can hardly be considered a result of random fault-slip data (see Table 4) [41]. TRM bulk stress tensors also explain more fault-slip data recorded in more SSs. As a result, the basic assumption of the inverse problem, i.e., that the faults slip independently, does not seem to be violated when the 'point' no longer occupies an infinitesimal size, as defined in physics, or the SS of limited spatial scale, as defined in geology, but refers to a geological region covering several tens of km^2. In the case of bulk stress tensors, the large number of fault-slip data recorded in different SSs, as well as the fact that the dataset, as a whole, represents a wide variation, both in the orientation and size of the measured faults, eliminate, as much as possible, any influence imposed by the fault structures themselves. Likewise, it eliminates any deviation between the local and regional kinematic field, e.g., in a thrust belt [89].

6. A New Paleostress History and Tectonic Implications

The type of deformation and paleostress history, and therefore, the late-orogenic deformation in the area north of Corsica Island, is poorly constrained and still under debate because it is an area where both the Pyrenean and western Alpine domains have come into contact since the Late Eocene [90]. Large-scale kinematics are dominated by the coeval effects of the ending collision of Iberia with Eurasia, the Apulia (Adria)-Eurasia convergence, and the north dipping subduction of Africa along the southern margin of the Iberian plate [45]. The overlap of several tectonic events [57,66], including the Early–Middle Miocene oceanic spreading of the Liguro-Provençal basin, the coeval 50° counterclockwise rotation [69] of the Ligurian Alps-TPB system [91], and the drifting of the Corsica-Sardinia block [92] make the area very complicated. Likewise, in the Ligurian Alps, there are two different scenarios, which, however, are based on studies having analyzed different structural data, thus making their comparison hard. The first is of [93], who suggested an E-W extensional regime with lithospheric thinning that was active since the Early Oligocene, and the second of ([58], and references therein), who suggested a transpressive regime for the tectonic evolution of the Ligurian Alps since the Oligocene.

Our paleostress analysis results are outlined in the following stress regimes:

$T1_{TRM}$ is a Transpression-(pure) Strike-Slip (TRP-SS) stress regime with a NW-SE trending σ_1 axis in a similar orientation to the Rupelian−Early Chattian event A of [32] and the Late Eocene–Early Oligocene compressional D3 event of [73]. On the other hand, [66] argued that the NW-SE compression is much younger, starting from the Late Miocene (post-Tortonian), as powered by the displacement of the Adriatic indenter against Eurasia and following the NE-SW-trending prevailing compressional regime that affected the Tertiary Piedmont Basin evolution in the Late Oligocene–Early Miocene. $T1_{TRM}$ stress tensor activated mainly ENE-WSW striking right-lateral, oblique-to-strike-slip contractional faults, but not reverse faults like those mentioned by [73]. If this is not due to fault sampling, these faults indicate that the ENE-WSW striking detachment shown in Figure 1 might have activated as a strike-slip fault under the $T1_{TRM}$ stress tensor. ENE-WSW trending faults, similar to those activated under the $T1_{TRM}$ stress tensor, limit the Tertiary Piedmont Valley in the area of Pra' Vallarino and north of Palo, as well as in the north-eastern boundary of the Voltri Massif [57], and they have been traced using photo-lineaments [74]. The activation of strike-slip instead of reverse faults in the region might indicate spatial variations of the driving stresses among the different regions.

$T2_{TRM}$ is an E-W Pure Extension (PE) stress regime that cannot be correlated with [32]'s proposed events. In other words, this extension has not been defined by [32]'s analysis that used both the FSA and Win-Tensor software. However, it fits well with the first brittle deformation phase (D4) of [57], which was a regional E-W to NE-SW extension developed in the metamorphic basement and the Tertiary Piedmont Basin in Rupelian–Early Chattian (~34–26 Ma), and led to the opening of the Liguro-Provencal Ocean, along with a counterclockwise rotation and drifting of Corsica-Sardinia [48]. The exhumation of the Voltri Massif to greenschist-facies, which took place approximately 34-30 Ma [94], has been attributed to E-W extension by [60]. The latter authors consider the E-W extension as an orogen parallel extension to the Southern Alps due to the advancing of the Western Alps to the west and the retreat of the Apennines slab. Moreover, [90] suggested such an extension as a post-orogenic one that truncated the Pyrenean thrusting and formed the Liguro-Provencal and Tyrrhenian basins [95], showing a major change in subduction dynamics [51].

$T3_{TRM}$ defines a TRN stress regime that cannot correlate with [32]'s events. On the other hand, it can be correlated with some N-S tensional stresses detected in several parts of the Tertiary Piedmont Basin, especially in its SE portion, though its timing relation with the other stress regimes is unclear [66]. These N-S tensional stresses are compatible with relatively small ENE-WSW to WNW-ESE trending normal faults mapped in the SE parts of the Tertiary Piedmont Basin [65,96,97], similar in strike to those activated by the $T3_{TRM}$ stress tensor (Figure 2d). [57] also mentioned a transtensional stress regime in the Late Chattian representing the transition from Early Oligocene rifting-related extension to the Early Miocene rotation-related transpression. In particular, [55] stated that this transtension marks the time when the Apennines start to 'pull' the southern Western Alps northeastward, producing a large shear zone (i.e., the Ligurian Alps-TPB) between the two chains. In this setting, the Tertiary Piedmont Basin acted as a strongly subsiding piggyback basin above rotating thrust sheets associated with the regional rotation caused by the oceanic spreading of the Liguro-Provençal basin, the Corsica-Sardinia drifting, and the eastward retreat of the northern Apennines slab.

$T4_{TRM}$ (ENE-WSW, TRP) and $T5_{TRM}$ (NNE-ESE, TRP) can be correlated with event B of [32], dated in Early Miocene (Aquitanian-early Burdigalian (?)) by them in the Late Oligocene–Early Miocene in the Tertiary Piedmont Basin by [66], and in Aquitanian–Serravallian (~23–12 Ma) by [57]. It is worth noticing that both $T4_{TRM}$ and $T5_{TRM}$ stress tensors reveal transpressive deformation. In addition, $T4_{TRM}$ and $T5_{TRM}$ stress tensors, with the former preceding the latter, fit well with the ~40° counterclockwise rotation of the σ_1 axes from ENE-WSW to NNE-SSW trends [73]. Similarly, the $T4_{TRM}$ and $T5_{TRM}$ stress tensors agree with the paleomagnetic data results that reveal ~50° of counterclockwise rotation for the Tertiary Piedmont Basin and the underlying Ligurian basement in the

Aquitanian–Serravallian times [69]. Field studies and seismic profile interpretations in the area provide strong evidence for transpressional structures and strike-slip flower structure geometries along E-W to ENE-striking faults that truncate and offset several unconformities bounding the Oligocene to lower Miocene sedimentary sequence, which in turn are sealed by Upper Miocene sediments [58,98].

The five (5) bulk stress tensors, $T1_{TRM}$ through $T5_{TRM}$ (Table 3), are well distinguished from each other and can be well correlated with the TRM site stress tensors (Table 2). Most TRM bulk stress tensors define TRP and TRN stress regimes instead of a (pure) strike-slip regime (SS). These stress regimes suggest that the deformation in the study area, which was part of the boundary between the orogenic belts of the Alps and Apennines, was not controlled by any large-scale (pure) strike-slip fault zone like the Sestri-Voltaggio Zone (Figure 1b), and was distributed along numerous and smaller strike-slip faults. Therefore, we consider the area to be a well-faulted relay ramp at a contractional overstep between larger-scale right-lateral strike-slip faults [99].

We have to note that estimated stress tensors of [32] are determined in some SSs from < 10 fault-slip data, and without any prior restoration or rotation of the recorded fault-slip data, although a ca. 50° of counterclockwise rotation for the Tertiary Piedmont Basin and the underlying Ligurian basement has been suggested in the Aquitanian–Serravallian times [69]. Since no absolute age information is available, as [32] pointed out, we compare the $T1_{TRM}$ through $T5_{TRM}$ stress tensors with the suggested deformational events of [32] and other published information concerning the deformation of the region, as described above in the five stress regime outlines.

Conclusively, the TRM application on the fault-slip data of [32] defines (a) a TRP-SS stress regime (T1) with NW-SE contraction, which can be correlated with the Late Eocene deformation of [73]; (b) an Oligocene E-W extensional regime (T2) fitting well with the E-W extension mentioned for the broader area due to a major change in subduction dynamics, perhaps as a consequence of collision and slowing down of the northward motion of Africa [51,89]; (c) an N-S transtension (T3), which has the σ_3 axis perpendicular to the σ_3 axis of the T2 stress regime; and (d) Miocene transpression (T4) with ENE-WNW contraction that changes to (e) transpression with NNE-SSW contraction (T5).

Based on these, we can argue that the Late Oligocene–Early Miocene marks a crucial period for the stress evolution in the broader area, since the plate convergence transferred eastwards from the Pyrenees collision zone to the Corsica-Sardinia trench system and the stress regime in the Ligurian Alps shifted gradually from an NW-SE to NE-SW direction of compression [57,90,92].

In particular, considering that the 50° counterclowise rotation occurred from the T4 to T5 stress regime, the T1 through T3 stress regimes should be restored to pre-rotational orientations. In that sense, the restored T1 represents a TRP-SS stress regime with contraction trending NNE-SSW. Such a contraction fits well with the NW-SE contraction in the Western Alps and its change to N-S towards the Pyrenees, placing the region along the Western Alps and Pyrenees (Figure 5a). The restored T2 stress regime is an extension trending NW-SE, similar to the extension dominating the Liguro-Provencal rifting (Figure 5b). The restored T3 stress regime, which is a transtension having a NE-SW trending σ_3 axis, i.e., perpendicular to the NW-SE T2 σ_3 axis, might be considered a local mutual permutation of the T2 stresses. The T4 and T5 stress regimes shown in Figure 5c,d indicate the gradual rotation that took place from the Early until the Middle Miocene. Since then, the area's configuration has been characterized by a gradual counterclockwise rotation and complex oblique and strike-slip deformation, as is documented in the upper crust via seismic tomography and earthquake alignments [100].

The change from the Oligocene extension to the Late Oligocene-Miocene compression and, in general, the stress reorganization in the Ligurian Alps, i.e., the internal area of the Northern Apennines and the Western Alps, can be attributed to the decrease in the retreating rate of the Apennines slab.

7. Conclusions

The present analysis shows that applying best-fit stress inversion methods to heterogeneous fault-slip data, even when complemented with sophisticated tools such as the Monte Carlo search method, does not ensure that the resolved stress tensors would represent the geologically real driving stress tensors. This conclusion is more profound when these methods are implemented on the fault-slip data of a limited number and at stations of limited spatial scale. The resolved best-fit site stress tensors are characterized by high diversity in stress orientation and at different stress ratios, with the tendency to define non-Andersonian (oblique) stress axes, especially when this approach is performed on a small number of recorded fault-slip data that might constitute a dynamically mixed fault-slip dataset. As a result, it is very hard and ambiguous to gather and to interpret fault-slip data under the same regional stress regime by considering only the site stress tensor solutions. On the contrary, the TRM when using additional fault-slip data separation criteria seems more promising when dealing with heterogeneous fault-slip data in finding enhanced Andersonian bulk stress tensors that describe the paleostress history and fault activation under the different faulting events, even in the absence of tectonostratigraphic criteria.

The TRM bulk paleostress tensors provide a more constrained paleostress history for the Voltri Massif and the Ligurian Alps, comprising five distinct stress regimes, which, after the restoration of the ~50° CCW rotation, comprise: (a) a transpression–strike-slip stress regime (T1) with NNE-SSW contraction in the Late Eocene, (b) an Oligocene NW-SE extensional regime (T2), which fits with the NW-SE extension documented for the broader area north of Corsica due to a significant change in subduction dynamics, (c) a transient, local, or ephemeral NE-SW transtension (T3), which might be considered to be a local mutual permutation of the T2 stresses, and (d) a Miocene transpression with a contraction that progressively shifted from ENE-WSW (T4) to NNE-SSW (T5). This paleostress history reflects the stress reorganization in the Ligurian Alps due to the combined effect of the transfer of the plate convergence eastwards, from the Pyrenees to the Corsica-Sardinia trench system, and the decrease in the retreating rate of the northern Apennines slab.

Author Contributions: Conceptualization, M.D.T. and P.G.N.; methodology, M.D.T.; software, M.D.T.; validation, M.D.T., P.G.N., S.A.K. and G.L.T.; data curation, M.D.T. and P.G.N.; writing—original draft preparation, M.D.T., P.G.N. and S.A.K.; writing—review and editing, M.D.T., P.G.N., S.A.K. and G.L.T. All authors have read and agreed to the published version of the manuscript.

Funding: This research received no external funding.

Informed Consent Statement: Not applicable.

Data Availability Statement: Not applicable.

Acknowledgments: We greatly appreciate the anonymous reviewers for their reviews and suggestions.

Conflicts of Interest: The authors declare no conflict of interest.

Appendix A

Table A1. List of the fault-slip data used in this study, derived from [32].

N	LABEL	FT_DIPD	FT_DIPA	RAKE	SOS	SS
1	FED_1	338	43	136	ND	SS2
2	FED_2	4	84	142	ND	SS2
3	FED_3	5	75	160	IS	SS2
4	FED_4	8	75	156	IS	SS2
5	FED_5	10	79	164	IS	SS2
6	FED_6	25	89	142	IS	SS2
7	FED_7	32	58	162	IS	SS2
8	FED_8	42	63	156	IS	SS2

Table A1. *Cont.*

N	LABEL	FT_DIPD	FT_DIPA	RAKE	SOS	SS
9	FED_9	31	86	165	IS	SS2
10	FED_10	40	75	160	IS	SS2
11	FED_11	207	85	41	NS	SS2
12	FED_12	24	64	165	IS	SS2
13	FED_13	24	71	155	IS	SS2
14	FED_14	35	66	154	ND	SS2
15	FED_15	24	82	154	IS	SS2
16	FED_16	26	77	161	IS	SS2
17	FED_17	30	77	21	NS	SS3
18	FED_18	35	79	158	IS	SS3
19	FED_19	231	75	168	IS	SS3
20	FED_20	237	62	97	ND	SS3
21	FED_21	244	61	30	ID	SS3
22	FED_22	244	47	14	ID	SS3
23	FED_23	246	40	12	NS	SS3
24	FED_24	68	5	168	ND	SS3
25	FED_25	90	30	90	N	SS3
26	FED_26	100	51	122	ND	SS3
27	FED_27	105	25	18	NS	SS3
28	FED_28	106	10	148	ND	SS3
29	FED_29	299	22	179	IS	SS3
30	FED_30	150	70	166	ND	SS3
31	FED_31	176	61	93	ND	SS3
32	FED_32	185	63	163	ND	SS3
33	FED_33	16	12	74	NS	SS3
34	FED_34	216	11	99	ND	SS3
35	FED_35	241	38	23	ID	SS3
36	FED_36	30	77	156	IS	SS3
37	FED_37	0	79	139	ND	SS3
38	FED_38	90	85	164	ND	SS6
39	FED_39	220	63	16	NS	SS6
40	FED_40	36	55	134	ND	SS6
41	FED_41	32	63	179	ND	SS6
42	FED_42	19	37	173	IS	SS6
43	FED_43	352	80	21	ID	SS6
44	FED_44	352	77	7	ID	SS6
45	FED_45	350	57	51	ID	SS6
46	FED_46	343	42	45	ID	SS6
47	FED_47	164	70	148	IS	SS6
48	FED_48	152	80	156	IS	SS6
49	FED_49	140	84	156	IS	SS6
50	FED_50	60	71	50	NS	SS6
51	FED_51	90	42	19	NS	SS7
52	FED_52	215	80	150	ND	SS7
53	FED_53	36	37	90	I	SS7
54	FED_54	228	69	150	ND	SS7
55	FED_55	240	35	162	ND	SS7
56	FED_56	250	59	168	ND	SS7
57	FED_57	75	25	81	ID	SS7
58	FED_58	88	43	38	ID	SS7
59	FED_59	288	65	77	NS	SS7
60	FED_60	289	80	179	ND	SS7
61	FED_61	296	32	175	IS	SS7
62	FED_62	120	51	1	ID	SS7
63	FED_63	122	84	155	ND	SS7
64	FED_64	130	45	7	ID	SS7
65	FED_65	130	48	174	ND	SS7

Table A1. *Cont.*

N	LABEL	FT_DIPD	FT_DIPA	RAKE	SOS	SS
66	FED_66	314	80	19	NS	SS7
67	FED_67	335	58	116	IS	SS7
68	FED_68	345	55	98	ND	SS7
69	FED_69	160	85	33	ID	SS7
70	FED_70	160	81	42	NS	SS7
71	FED_71	157	42	170	ND	SS7
72	FED_72	165	77	23	ID	SS7
73	FED_73	166	76	129	ND	SS7
74	FED_74	171	69	38	NS	SS7
75	FED_75	8	71	62	NS	SS7
76	FED_76	190	62	35	NS	SS7
77	FED_77	192	85	14	ID	SS7
78	FED_78	194	76	159	ND	SS7
79	FED_79	195	77	159	ND	SS7
80	FED_80	0	71	36	NS	SS7
81	FED_81	215	41	77	NS	SS7
82	FED_82	310	73	167	ND	SS7
83	FED_83	260	50	54	ID	SS11
84	FED_84	270	54	59	ID	SS11
85	FED_85	276	74	15	ID	SS11
86	FED_86	290	80	87	NS	SS11
87	FED_87	295	46	165	IS	SS11
88	FED_88	302	59	2	NS	SS11
89	FED_89	143	85	29	NS	SS11
90	FED_90	178	72	54	NS	SS11
91	FED_91	27	79	169	ND	SS11
92	FED_92	61	51	64	NS	SS11

Explanation: N: Number; FT_DIPD: Fault Dip Direction; FT_DIPA: Fault Dip Angle; SOS: Sense-of-Shear (N: Normal, I: Inverse, D: Dextral, S: Sinistral); SS: Structural Station. Rake is given in values 0 to 180° in a clockwise sense.

References

1. Etchecopar, A.; Vasseur, G.; Daignieres, M. An inverse problem in microtectonics for the determination of stress tensors from fault striation analysis. *J. Struct. Geol.* **1981**, *3*, 51–65. [CrossRef]
2. Angelier, J. Fault slip analysis and palaeostress reconstruction. In *Continental Deformation*; Pergamon Press: Oxford, UK, 1994; pp. 53–100.
3. Carey, E.; Brunier, B. Analyse théorique et numérique d'un modéle mécanique élémentaire appliqué é I' étude d'une population de failles. *C. R. Acad. Sci. Paris* **1974**, *279*, 891–894.
4. Angelier, J.; Goguel, J. Sur une méthode simple de détermination des axes principaux des contraintes pour une population de failles. *C. R. Acad. Sci. Paris* **1979**, *288*, 307–310.
5. Angelier, J. Determination of the mean principal directions of stresses for a given fault population. *Tectonophysics* **1979**, *56*, T17–T26. [CrossRef]
6. Armijo, R.; Carey, E.; Cisternas, A. The inverse problem in microtectonics and the separation of tectonic phases. *Tectonophysics* **1982**, *82*, 145–160. [CrossRef]
7. Angelier, J. Tectonic analysis of fault slip data sets. *J. Geophys. Res. Earth Surf.* **1984**, *89*, 5835–5848. [CrossRef]
8. Huang, Q. Computer-based method to separate heterogeneous sets of fault-slip data into sub-sets. *J. Struct. Geol.* **1988**, *10*, 297–299. [CrossRef]
9. Angelier, J. From orientation to magnitudes in paleostress determinations using fault slip data. *J. Struct. Geol.* **1989**, *11*, 37–50. [CrossRef]
10. Hardcastle, K.C. Possible paleostress tensor configurations derived from fault-slip data in eastern Vermont and western New Hampshire. *Tectonics* **1989**, *8*, 265–284. [CrossRef]
11. Gephart, J.W. FMSI: A fortran program for inverting fault/slickenside and earthquake focal mechanism data to obtain the regional stress tensor. *Comput. Geosci.* **1990**, *16*, 953–989. [CrossRef]
12. Will, T.M.; Powell, R. A robust approach to the calculation of paleostress fields from fault plane data. *J. Struct. Geol.* **1991**, *13*, 813–821. [CrossRef]
13. Twiss, R.J.; Unruh, J.R. Analysis of fault slip inversions: Do they constrain stress or strain rate? *J. Geophys. Res. Earth Surf.* **1998**, *103*, 12205–12222. [CrossRef]
14. Sperner, B.; Zweigel, P. A plea for more caution in fault–slip analysis. *Tectonophysics* **2010**, *482*, 29–41. [CrossRef]

15. Bott, M.H.P. The Mechanics of Oblique Slip Faulting. *Geol. Mag.* **1959**, *96*, 109–117. [CrossRef]
16. Anderson, E.M. The dynamics of faulting. *Trans. Edinb. Geol. Soc.* **1905**, *8*, 387–402. [CrossRef]
17. Wallace, R.E. Geometry of shearing stress and relation to faulting. *J. Geol.* **1951**, *59*, 118–130. [CrossRef]
18. Pollard, D.D.; Saltzer, S.D.; Rubin, A.M. Stress inversion methods: Are they based on faulty assumptions? *J. Struct. Geol.* **1993**, *15*, 1045–1054. [CrossRef]
19. Dupin, J.-M.; Sassi, W.; Angelier, J. Homogeneous stress hypothesis and actual fault slip: A distinct element analysis. *J. Struct. Geol.* **1993**, *15*, 1033–1043. [CrossRef]
20. Roberts, G.P. Variation in fault-slip directions along active and segmented normal fault systems. *J. Struct. Geol.* **1996**, *18*, 835–845. [CrossRef]
21. Maerten, L. Variation in slip on intersecting normal faults: Implications for paleostress inversion. *J. Geophys. Res. Earth Surf.* **2000**, *105*, 25553–25565. [CrossRef]
22. Célérier, B. Remarks on the relationship between the tectonic regime, the rake of the slip vectors, the dip of the nodal planes, and the plunges of the P, B, and T axes of earthquake focal mechanisms. *Tectonophysics* **2010**, *482*, 42–49. [CrossRef]
23. Célérier, B.; Etchecopar, A.; Bergerat, F.; Vergely, P.; Arthaud, F.; Laurent, P. Inferring stress from faulting: From early concepts to inverse methods. *Tectonophysics* **2012**, *581*, 206–219. [CrossRef]
24. Tranos, M.D. Slip preference on pre-existing faults: A guide tool for the separation of heterogeneous fault-slip data in extensional stress regimes. *Tectonophysics* **2012**, *544–545*, 60–74. [CrossRef]
25. Tranos, M.D. The TR method: The use of slip preference to separate heterogeneous fault-slip data in compressional stress regimes. The surface rupture of the 1999 Chi-Chi Taiwan earthquake as a case study. *Tectonophysics* **2013**, *608*, 622–641. [CrossRef]
26. Tranos, M.D. Slip preference analysis of faulting driven by strike-slip Andersonian stress regimes: An alternative explanation of the Rhodope metamorphic core complex (northern Greece). *J. Geol. Soc.* **2016**, *174*, 129–141. [CrossRef]
27. Kokkalas, S.; Doutsos, T. Strain-dependent stress field and plate motions in the south-east Aegean region. *J. Geodyn.* **2001**, *32*, 311–332. [CrossRef]
28. Lacombe, O. Do fault slip data inversions actually yield "paleostresses" that can be compared with contemporary stresses? A critical discussion. *Comptes Rendus Geosci.* **2012**, *344*, 159–173. [CrossRef]
29. Kounov, A.; Burg, J.-P.; Bernoulli, D.; Seward, D.; Ivanov, Z.; Dimov, D.; Gerdjikov, I. Paleostress analysis of Cenozoic faulting in the Kraishte area, SW Bulgaria. *J. Struct. Geol.* **2011**, *33*, 859–874. [CrossRef]
30. Tranos, M.D. Strymon and Strymonikos Gulf basins (Northern Greece): Implications on their formation and evolution from faulting. *J. Geodyn.* **2011**, *51*, 285–305. [CrossRef]
31. Delvaux, D.; Kervyn, F.; Macheyeki, A.S.; Temu, E.B. Geodynamic significance of the TRM segment in the East African Rift (W-Tanzania): Active tectonics and paleostress in the Ufipa plateau and Rukwa basin. *J. Struct. Geol.* **2012**, *37*, 161–180. [CrossRef]
32. Federico, L.; Crispini, L.; Vigo, A.; Capponi, G. Unravelling polyphase brittle tectonics through multi-software fault-slip analysis: The case of the Voltri Unit, Western Alps (Italy). *J. Struct. Geol.* **2014**, *68*, 175–193. [CrossRef]
33. Assie, K.R.; Wang, Y.; Tranos, M.D.; Ma, H.; Kouamelan, K.S.; Brantson, E.T.; Zhou, L.; Ketchaya, Y.B. Late Cenozoic faulting deformation of the Fanshi Basin (northern Shanxi rift, China), inferred from palaeostress analysis of mesoscale fault-slip data. *Geol. Mag.* **2022**, 1–17. [CrossRef]
34. Bellier, O.; Zoback, M.L. Recent state of stress change in the Walker Lane zone, western Basin and Range province, United States. *Tectonics* **1995**, *14*, 564–593. [CrossRef]
35. Tranos, M.D. Faulting of Lemnos Island; a mirror of faulting of the North Aegean Trough (Northern Greece). *Tectonophysics* **2009**, *467*, 72–88. [CrossRef]
36. Liesa, C.L.; Lisle, R.J. Reliability of methods to separate stress tensors from heterogeneous fault-slip data. *J. Struct. Geol.* **2004**, *26*, 559–572. [CrossRef]
37. Hardcastle, K.C.; Hills, L.S. BRUTE3 and SELECT: QUICKBASIC 4 programs for determination of stress tensor configurations and separation of heterogeneous populations of fault-slip data. *Comput. Geosci.* **1991**, *17*, 23–43. [CrossRef]
38. Nemcok, M.; Richard, J.L. A stress inversion procedure for polyphase fault/slip data sets. *J. Struct. Geol.* **1995**, *17*, 1445–1453. [CrossRef]
39. Fry, N. Striated faults: Visual appreciation of their constraint on possible paleostress tensors. *J. Struct. Geol.* **1999**, *21*, 7–21. [CrossRef]
40. Shan, Y.; Suen, H.; Lin, G. Separation of polyphase fault/slip data: An objective-function algorithm based on hard division. *J. Struct. Geol.* **2003**, *25*, 829–840. [CrossRef]
41. Orife, T.; Lisle, R.J. Assessing the statistical significance of palaeostress estimates: Simulations using random fault-slips. *J. Struct. Geol.* **2006**, *28*, 952–956. [CrossRef]
42. Célérier, B. Fault Slip and Stress Analysis (FSA). Available online: http://www.celerier.gm.univ-montp2.fr/software/dcmt/fsa/fsa.html (accessed on 6 October 2022).
43. Delvaux, D. *Win-Tensor Program*, Version 3.0 and Above; Royal Museum for Central Africa: Tervuren, Belgium, 2022. Available online: https://www.damiendelvaux.be/Tensor/WinTensor/win-tensor.html(accessed on 6 October 2022).
44. Tranos, M.D. TR method (TRM): A separation and stress inversion method for heterogeneous fault-slip data driven by Andersonian extensional and compressional stress regimes. *J. Struct. Geol.* **2015**, *79*, 57–74. [CrossRef]

45. Rosenbaum, G.; Lister, G.S.; Duboz, C. Reconstruction of the tectonic evolution of the western Mediterranean since the Oligocene. *J. Virtual Explor.* **2002**, *8*, 107–130. [CrossRef]
46. Spakman, W.; Wortel, R. A Tomographic View on Western Mediterranean Geodynamics. In *The TRANSMED Atlas. The Mediterranean Region from Crust to Mantle: Geological and Geophysical Framework of the Mediterranean and the Surrounding Areas*; Cavazza, W., Roure, F., Spakman, W., Stampfli, G.M., Ziegler, P.A., Eds.; Springer: Berlin/Heidelberg, Germany, 2004; pp. 31–52.
47. Butler, R.W.H. Thrust tectonics, deep structure and crustal subduction in the Alps and Himalayas. *J. Geol. Soc.* **1986**, *143*, 857–873. [CrossRef]
48. Platt, J.P.; Behrmann, J.H.; Cunningham, P.C.; Dewey, J.F.; Helman, M.; Parish, M.; Shepley, M.G.; Wallis, S.; Western, P.J. Kinematics of the Alpine arc and the motion history of Adria. *Nature* **1989**, *337*, 158–161. [CrossRef]
49. Ford, M.; Duchêne, S.; Gasquet, D.; Vanderhaeghe, O. Two-phase orogenic convergence in the external and internal SW Alps. *J. Geol. Soc.* **2006**, *163*, 815–826. [CrossRef]
50. Patacca, E.; Sartori, R.; Scandone, P. Tyrrhenian Basin and Apennines. Kinematic Evolution and Related Dynamic Constraints. In *Recent Evolution and Seismicity of the Mediterranean Region*; Boschi, E., Mantovani, E., Morelli, A., Eds.; Springer: Dordrecht, The Netherlands, 1993; pp. 161–171.
51. Jolivet, L.; Faccenna, C. Mediterranean extension and the Africa-Eurasia collision. *Tectonics* **2000**, *19*, 1095–1106. [CrossRef]
52. Strating, E.H.H. The evolution of the Piemonte–Ligurian Ocean. A structural study of ophiolite complexes in Liguria (NW Italy). *Geol. Ultraiectina* **1991**, *74*, 145.
53. Capponi, G.; Crispini, L.; Federico, L.; Malatesta, C. Geology of the Eastern Ligurian Alps: A review of the tectonic units. *Ital. J. Geosci.* **2016**, *135*, 157–169. [CrossRef]
54. Rovereto, G. Liguria Geologica. *Mem. Soc. Geol. It.* **1939**, *2*, 147–155.
55. Görler, K.; Ibbeken, H. Die Bedeutung der Zone Sestri-voltaggio Als Grenze Zwischen Alpen und Apennin. *Geol. Rundsch.* **1964**, *53*, 73–84. [CrossRef]
56. Crispini, L.; Capponi, G. Tectonic evolution of the Voltri Group and Sestri Voltaggio Zone (southern limit of the NW Alps): A review. *Ofioliti* **2001**, *26*, 161–164.
57. Maino, M.; Decarlis, A.; Felletti, F.; Seno, S. Tectono-sedimentary evolution of the Tertiary Piedmont Basin (NW Italy) within the Oligo-Miocene central Mediterranean geodynamics. *Tectonics* **2013**, *32*, 593–619. [CrossRef]
58. Capponi, G.; Crispini, L.; Federico, L.; Piazza, M.; Fabbri, B. Late Alpine tectonics in the Ligurian Alps: Constraints from the Tertiary Piedmont Basin conglomerates. *Geol. J.* **2009**, *44*, 211–224. [CrossRef]
59. Federico, L.; Spagnolo, C.; Crispini, L.; Capponi, G. Fault-slip analysis in the metaophiolites of the Voltri Massif: Constraints for the tectonic evolution at the Alps/Apennine boundary. *Geol. J.* **2008**, *44*, 225–240. [CrossRef]
60. Vignaroli, G.; Faccenna, C.; Rossetti, F. Retrogressive fabric development during exhumation of the Voltri Massif (Ligurian Alps, Italy): Arguments for an extensional origin and implications for the Alps–Apennines linkage. *Int. J. Earth Sci.* **2008**, *98*, 1077–1093. [CrossRef]
61. Bally, A.W.; Burbi, L.; Cooper, C.; Ghelardoni, R. Balanced sections and seismic reflection profiles across the Central Apennines. *Mem. Soc. Geol. It.* **1986**, *35*, 257–310.
62. Bernoulli, D. Mesozoic-Tertiary carbonate platforms, slopes and basins of the external Apennines and Sicily. In *Anatomy of an Orogen: The Apennines and Adjacent Mediterranean Basins*; Vai, G.B., Martini, I.P., Eds.; Springer: Dordrecht, The Netherlands, 2001; pp. 307–325.
63. Cavazza, W.; Wezel, F.C. The Mediterranean region- a geological primer. *Episodes* **2003**, *26*, 160–168. [CrossRef] [PubMed]
64. Molli, G.; Crispini, L.; Malusà, M.; Mosca, P.; Piana, F.; Federico, L. Geology of the Northern Apennine-Western Alps junction area: A regional review. *J. Virtual Explor.* **2010**, *36*, 1–49. [CrossRef]
65. Mutti, E.; Papani, L.; Di Biase, D.; Davoli, G.; Mora, S.; Segadelli, S.; Tinterri, R. Il Bacino Terziario Epimesoalpino e le sue implicazioni sui rapporti tra Alpi ed Appennino. *Mem. Di Sci. Geol.* **1995**, *47*, 217–244.
66. Felletti, F. Complex bedding geometries and facies associations of the turbiditic fill of a confined basin in a transpressive setting (Castagnola Fm., Tertiary Piedmont Basin, NW Italy). *Sedimentology* **2002**, *49*, 645–667. [CrossRef]
67. Carrapa, B.; Bertotti, G.; Krijgsman, W. Subsidence, stress regime and rotation(s) of a tectonically active sedimentary basin within the western Alpine Orogen: The Tertiary Piedmont Basin (Alpine domain, NW Italy). *Geol. Soc. London Spec. Publ.* **2003**, *208*, 205–227. [CrossRef]
68. Piana, F.; Tallone, S.; Cavagna, S.; Conti, A. Thrusting and faulting in metamorphic and sedimentary units of Ligurian Alps: An example of integrated field work and geochemical analyses. *Int. J. Earth Sci.* **2006**, *95*, 413–430. [CrossRef]
69. Maffione, M.; Speranza, F.; Faccenna, C.; Cascella, A.; Vignaroli, G.; Sagnotti, L. A synchronous Alpine and Corsica-Sardinia rotation. *J. Geophys. Res. Solid Earth* **2008**, *113*, 1–25. [CrossRef]
70. Chiesa, S.; Cortesogno, L.; Forcella, F.; Galli, M.; Messiga, B.; Pasquare, G.; Pedemonte, G.; Piccardo, G.; Rossi, P. Assetto strutturale ed interpretazione geodinamica del Gruppo di Voltri. *Boll. Della Soc. Geol. Ital.* **1975**, *94*, 555–581.
71. Capponi, G.; Crispini, L.; Silvestri, R.; Vigo, E. The role of Early Miocene thrust tectonics in the structural arrangement of the Voltri Group (Ligurian Alps, Italy): Evidence from the Bandita area. *Ofioliti* **1999**, *24*, 13–19.
72. Strating, E.H.H.; van Wamel, W.A.; Vissers, R.L.M. Some constraints on the kinematics of the Tertiary Piemonte Basin (northwest Italy). *Tectonophysics* **1991**, *198*, 47–51. [CrossRef]

73. Spagnolo, C.; Crispini, L.; Capponi, G. From Alpine to Apennine orogeny: Structural records in the Voltri Massif (Ligurian Alps, Italy). *Geodin. Acta* **2007**, *20*, 21–35. [CrossRef]
74. Crispini, L.; Federico, L.; Capponi, G.; Spagnolo, C. Late orogenic transpressional tectonics in the «Ligurian Knot». *Ital. J. Geosci.* **2009**, *128*, 433–441. [CrossRef]
75. Marini, M. Le deformazioni fragili del Pliocene Ligure. Implicazioni nella geodinamica alpina. *Mem. Soc. Geol. Ital* **1987**, *29*, 157–169.
76. Jolivet, L.; Faccenna, C.; Goffé, B.; Burov, E.; Agard, P. Subduction tectonics and exhumation of high-pressure metamorphic rocks in the Mediterranean orogens. *Am. J. Sci.* **2003**, *303*, 353–409. [CrossRef]
77. Delvaux, D.; Sperner, B. Stress tensor inversion from fault kinematic indicators and focal mechanism data: The TENSOR program. *Geol. Soc. Lond. Spec. Publ.* **2003**, *212*, 75–100. [CrossRef]
78. Morris, A.; Ferrill, D.A.; Henderson, D.B. Slip-tendency analysis and fault reactivation. *Geology* **1996**, *24*, 275–278. [CrossRef]
79. Tranos, M.D.; Kachev, V.N.; Mountrakis, D.M. Transtensional origin of the NE–SW Simitli basin along the Strouma (Strymon) Lineament, SW Bulgaria. *J. Geol. Soc.* **2008**, *165*, 499–510. [CrossRef]
80. Pollard, D.; Fletcher, R.C. *Fundamentals of Structural Geology*, 1st ed.; Cambridge University Press: Cambridge, UK, 2005.
81. Michael, A.J. Determination of stress from slip data: Faults and folds. *J. Geophys. Res. Solid Earth* **1984**, *89*, 11517–11526. [CrossRef]
82. Michael, A.J. Use of focal mechanisms to determine stress: A control study. *J. Geophys. Res. Solid Earth* **1987**, *92*, 357–368. [CrossRef]
83. Tranos, M.D. The use of Stress Tensor Discriminator Faults in separating heterogeneous fault-slip data with best-fit stress inversion methods. *J. Struct. Geol.* **2017**, *102*, 168–178. [CrossRef]
84. Tranos, M.D. The use of Stress Tensor Discriminator Faults in separating heterogeneous fault-slip data with best-fit stress inversion methods. II. Compressional stress regimes. *J. Struct. Geol.* **2018**, *107*, 153–162. [CrossRef]
85. Tranos, M.D. Is the Monte Carlo search method efficient for a paleostress analysis of natural heterogeneous fault-slip data? An example from the Kraishte area, SW Bulgaria. *J. Struct. Geol.* **2018**, *116*, 178–188. [CrossRef]
86. Lisle, R.J.; Orife, T.O.; Arlegui, L.; Liesa, C.; Srivastava, D.C. Favoured states of palaeostress in the Earth's crust: Evidence from fault-slip data. *J. Struct. Geol.* **2006**, *28*, 1051–1066. [CrossRef]
87. Paradisopoulou, P.M.; Karakostas, V.G.; Papadimitriou, E.; Tranos, M.D.; Papazachos, C.B.; Karakaisis, G.F. Microearthquake study of the broader Thessaloniki area (Northern Greece). *Ann. Geophys.* **2006**, *49*, 1081–1093. [CrossRef]
88. Anderson, E.M. *The Dynamics of Faulting*; Olivier and Boyd: Edinburgh, UK, 1942.
89. Chatzaras, V.; Xypolias, P.; Kokkalas, S.; Koukouvelas, I. Tectonic evolution of a crustal-scale oblique ramp, Hellenides thrust belt, Greece. *J. Struct. Geol.* **2013**, *57*, 16–37. [CrossRef]
90. Lacombe, O.; Jolivet, L. Structural and kinematic relationships between Corsica and the Pyrenees-Provence domain at the time of the Pyrenean orogeny. *Tectonics* **2005**, *24*, TC1003. [CrossRef]
91. Vanossi, M.; Sogno, L.C.; Galbiati, B.; Messiga, B.; Piccardo, G.; Vannucci, R. Geologia delle Alpi Liguri: Dati, problemi, ipotesi. *Mem. Della Soc. Geol. Ital.* **1984**, *28*, 5–75.
92. Gattacceca, J.; Deino, A.; Rizzo, R.; Jones, D.S.; Henry, B.; Beaudoin, B.; Vadeboin, F. Miocene rotation of Sardinia: New paleomagnetic and geochronological constraints and geodynamic implications. *Earth Planet. Sci. Lett.* **2007**, *258*, 359–377. [CrossRef]
93. Vignaroli, G.; Faccenna, C.; Jolivet, L.; Piromallo, C.; Rossetti, F. Subduction polarity reversal at the junction between the Western Alps and the Northern Apennines, Italy. *Tectonophysics* **2008**, *450*, 34–50. [CrossRef]
94. Starr, P.G.; Broadwell, K.S.; Dragovic, B.; Scambelluri, M.; Haws, A.A.; Caddick, M.J.; Smye, A.J.; Baxter, E.F. The subduction and exhumation history of the Voltri Ophiolite, Italy: Evaluating exhumation mechanisms for high-pressure metamorphic massifs. *Lithos* **2020**, *376–377*, 105767. [CrossRef]
95. Brunet, C.; Monié, P.; Jolivet, L.; Cadet, J.P. Migration of compression and extension in the Tyrrhenian Sea, insights from 40Ar/39Ar ages on micas along a transect from Corsica to Tuscany. *Tectonophysics* **2000**, *321*, 127–155. [CrossRef]
96. Bernini, M.; Zecca, M. Le deformazioni nelle Formazioni di Molare e di Rocchetta (Oligocene-Miocene inferiore) della regione di Mioglia (SV) (Margine Sud del Bacino Terziario Piemontese. *Atti Tic. Sc. Terra* **1990**, *33*, 1–10.
97. Gelati, R.; Gnaccolini, M. Synsedimentary tectonics and sedimentation in the tertiary Piedmont Basin, northwestern Italy. *Riv. Ital. Paleontol. Stratigr.* **1998**, *104*, 193–214.
98. Mosca, P.; Polino, R.; Rogledi, S.; Rossi, M. New data for the kinematic interpretation of the Alps–Apennines junction (Northwestern Italy). *Int. J. Earth Sci.* **2010**, *99*, 833–849. [CrossRef]
99. Peacock, D.C.P.; Sanderson, D.J. Strike-slip relay ramps. *J. Struct. Geol.* **1995**, *17*, 1351–1360. [CrossRef]
100. Eva, E.; Malusà, M.G.; Solarino, S. Seismotectonics at the Transition Between Opposite-Dipping Slabs (Western Alpine Region). *Tectonics* **2020**, *39*, e2020TC006086. [CrossRef]